Soft Matter

PAPER

View Article Online
View Journal | View Issue

Cite this: *Soft Matter*, 2024, **20**, 7865

Emergent mesoscale correlations in active solids with noisy chiral dynamics†

Amir Shee,[a] Silke Henkes*[b] and Cristián Huepe*[acd]

We present the linear response theory for an elastic solid composed of active Brownian particles with intrinsic individual chirality, deriving both a normal mode formulation and a continuum elastic formulation. Using this theory, we compute analytically the velocity correlations and energy spectra under different conditions, showing an excellent agreement with simulations. We generate the corresponding phase diagram, identifying chiral and achiral disordered regimes (for high chirality or noise levels), as well as chiral and achiral states with mesoscopic-range order (for low chirality and noise). The chiral ordered states display mesoscopic spatial correlations and oscillating time correlations, but no wave propagation. In the high chirality regime, we find a peak in the elastic energy spectrum that leads to a non-monotonic behavior with increasing noise strength that is consistent with the emergence of the 'hammering state' recently identified in chiral glasses. Finally, we show numerically that our theory, despite its linear response nature, can be applied beyond the idealized homogeneous solid assumed in our derivations. Indeed, by increasing the level of activity, we show that it remains a good approximation of the system dynamics until just below the melting transition. In addition, we show that there is still an excellent agreement between our analytical results and simulations when we extend our results to heterogeneous solids composed of mixtures of active particles with different intrinsic chirality and noise levels. The derived linear response theory is therefore robust and applicable to a broad range of real-world active systems. Our work provides a thorough analytical and numerical description of the emergent states in a densely packed system of chiral self-propelled Brownian disks, thus allowing a detailed understanding of the phases and dynamics identified in a minimal chiral active system.

Received 9th August 2024,
Accepted 17th September 2024

DOI: 10.1039/d4sm00958d

rsc.li/soft-matter-journal

1 Introduction

Chirality is a fundamental property of most chemical, physical, and biological systems that is expected to naturally occur in active matter. Indeed, in the context of self-propelled particles, chiral motion has been shown to spontaneously arise due to asymmetries in the self-propulsion forces or in the particle geometry,[1–4] or as a result of interactions with external fields.[5,6]

The relationship between activity and chirality has been considered in multiple contexts. Chiral motion has been observed experimentally in active biomolecules[7] such as proteins,[8] in microtubules,[9] and in single cells, including bacteria[10–12] and sperm cells.[13,14] It has been studied theoretically for single circle swimmers,[15–23] for the clockwise circular dynamics of *E. coli*,[24,25] and for circular and helical motion under chemical gradients.[26,27] Groups of chiral swimmers have been shown to display unique forms of collective dynamics, whether chirality resulted from shape asymmetry,[28–32] mass distribution,[33] or catalysis coating.[34] Chiral particles can also display a range of non-equilibrium phases, including a gas of spinners and aster-like vortices, rotating flocks with either polar or nematic alignment,[32] and states displaying phase separation, swarming, or oscillations, among others.[35]

Several theoretical studies have shown that chirality can strongly affect the collective states that are typically found in achiral active systems. In cases with explicit mutual alignment interactions (as in the Vicsek model), it has been shown that chiral polar swimmers display stronger flocking behavior than achiral ones, with higher levels of polarization in the ordered phase,[36] and that large rotating clusters with enhanced size and shape fluctuations can emerge.[37] In cases with other types of angular interactions, a marked attenuation of motility-induced phase separation (MIPS),[38] the emergence of vortex arrays,[39] and chirality-triggered oscillatory dynamic clustering[40] have

[a] *Northwestern Institute on Complex Systems and ESAM, Northwestern University, Evanston, IL 60208, USA*
[b] *Lorentz Institute for Theoretical Physics, LION, Leiden University, P.O. Box 9504, 2300 RA Leiden, The Netherlands. E-mail: shenkes@lorentz.leidenuniv.nl*
[c] *School of Systems Science, Beijing Normal University, Beijing, People's Republic of China*
[d] *CHuepe Labs, 2713 West August Blvd #1, Chicago, IL 60622, USA. E-mail: cristian@northwestern.edu*

† Electronic supplementary information (ESI) available. See DOI: https://doi.org/10.1039/d4sm00958d

been observed. Chirality has also been found to affect the collective states of active particles without explicit alignment interactions. For instance, chiral active Brownian particles can suppress conventional MIPS due to the formation of dynamical clusters that disrupt the MIPS clusters,[41,42] and a quantitative field theory was developed to account for this suppression.[43] Furthermore, chiral active particles with fast rotation have been found to form non-equilibrium hyperuniform fluids.[44,45]

Novel collective states have also been identified in inhomogeneous systems that combine different types of activity and chirality. For example, in a low-density environment, binary mixtures of passive and active chiral self-propelled particles exhibit transitions from mixed gels to rotating passive clusters, and then to homogeneous fluids.[46] In addition, a mixture of active particles with different chirality frequencies can create complex combinations of clusters of different sizes, rotating at different rates.[47] At low density, active chiral mixtures with opposite chiralities can also give rise to spontaneous demixing.[48] Moreover, the combination of chiral and achiral swarming coupled oscillators leads to a range of novel behaviors, such as the formation of vortex lattices, pulsating clusters, or interacting phase waves.[49]

Although most research on chiral systems has focused on liquid- and gas-like states, solid chiral active states have been found to naturally arise in systems such as groups of spinning magnetic particles[50] or of starfish oocytes[51] when hydrodynamic torque couplings are included, resulting in active chiral crystals.[51–57] The interactions in these cases can be cast as nonreciprocal odd-elastic viscous active couplings, to place them within the framework of odd active matter.[58] The elastic coefficients then acquire non-symmetric contributions, and the resulting lack of energy conservation, as well as the polarity-position coupling, allow for wave propagation and work cycles. Here we will consider a different class of systems, focusing on a minimal model of solid ''dry'' active matter, where chirality is introduced as part of the active forces, not as an active stress. Since in this case there are no action–reaction effects in the active driving, activity cannot be recast as part of the stress tensor or in the elastic coefficients, and an odd-elasticity framework is not applicable.

Solid and dense active systems without chirality have received significant interest in recent years. On one hand, the emergent states of self-propelled particles with self-alignment interactions have been studied in multiple contexts.[59–64] On the other hand, various dense and glassy active matter systems[65–68] without any alignment interaction have been described theoretically, using active Brownian particles in ref. 69–81 and active Ornstein–Uhlenbeck particles in ref. 82–88. However, their chiral counterparts have so far received limited attention. In one study, Debets *et al.*[89] examined the glassy dynamics of chiral active Brownian particles, showing that they exhibit highly nontrivial states and a non-monotonic behavior of the diffusion constant *versus* noise at high chirality that we also find in our system. In another study, Caprini *et al.*[90] showed the emergence of rotating and oscillating states, deriving an analytical phase diagram by applying an active solid approach similar to that presented below, but in a different context. Lastly, in recent work, Kuroda *et al.*[91] used linear elasticity theory to deduce the presence of long-range translational order in active chiral crystals with zero noise.

In this paper, we investigate the collective dynamics of chiral active Brownian disks with elastic repulsive interactions at high densities, in the solid state. We identify and describe the different phases, finding an emergent mesoscopic length scale that can display or not oscillatory time correlations, depending on the ratio of chiral motion to rotational noise. We derive an analytical active solid theory to describe these phases, using a normal mode approach and a continuum elasticity approach, both of which match our simulations. In addition, we show that these results remain valid well into the nonlinear regime, just below the melting transition, and inform the dynamics of the fluid state. They also extend to different kinds of active binary mixtures, including mixtures of chiral and achiral particles, of chiral particles with different rotational speeds, and of chiral particles with different levels of rotational diffusion.

The paper is organized as follows. In Section 2, we describe our two-dimensional active solid model of densely packed self-propelled disks with elastic interactions and intrinsic individual chirality. In Section 3, we overview the phase space of dynamical regimes as a function of chirality and rotational diffusion. In Section 4, we present our analytical results. We first calculate the orientation autocorrelation functions using a Fokker–Planck approach; then describe the normal mode formalism for active solids, calculating the average energy per mode and the spatial velocity correlations; and finally describe the continuum elastic formulation. In Section 5, we characterize the dynamics described by our results and compare them to simulations. In Section 6, we examine the melting regime by increasing the level of activity. In Section 7, we extend our results to heterogeneous mixtures of disks with different levels of activity and chirality. Finally, Section 8 presents our conclusions.

2 Model

We consider a system of N densely packed soft chiral self-propelled disks following overdamped dynamics in a two dimensional periodic box of size $L \times L$. Disregarding passive translational diffusion, the dynamics of the position $\mathbf{r}_i \equiv (x_i,y_i)$ and of the heading direction or orientational unit vector $\hat{n}_i \equiv (\cos(\theta_i),\sin(\theta_i))$ of the i-th disk will be given by

$$\dot{\mathbf{r}}_i = v_0\hat{n}_i + \mu\mathbf{F}_i, \tag{1}$$

$$\dot{\hat{n}}_i = \left[\Omega + \sqrt{2D_r}\eta_i(t)\right]\hat{n}_i^{\perp}. \tag{2}$$

Here, v_0 is the self-propulsion speed, μ is the mobility (inverse damping coefficient), Ω is the chiral angular speed (often referred to as chirality) of the disks, D_r is their rotational diffusion coefficient, and $\hat{n}_i^{\perp}$ is a unit vector perpendicular to $\hat{n}_i$. Noise is introduced through the random variable $\eta_i(t)$,

following Gaussian white noise with $\langle \eta_i(t) \rangle = 0$ and $\langle \eta_i(t)\eta_j(t') \rangle = \delta_{ij}\delta(t - t')$. The sum of all contact forces over disk i is $\mathbf{F}_i = \sum_{j \in S_i} \mathbf{f}_{ij}$, where S_i is the set of indexes of all disks that overlap disk i. These forces are modeled as linear repulsion, with $\mathbf{f}_{ij} = k(|\mathbf{r}_{ij}| - l_0)\mathbf{r}_{ij}/|\mathbf{r}_{ij}|$ if $|\mathbf{r}_{ij}| \leq l_0$ and $\mathbf{f}_{ij} = 0$ otherwise, were $\mathbf{r}_{ij} = \mathbf{r}_j - \mathbf{r}_i$ and $l_0 = 2r_0$ is the equilibrium center-to-center distance between two neighboring disks of radius r_0. We note that, in real-world scenarios, Ω and D_r cannot be exactly the same for all disks. In Section 7, we thus conduct a comprehensive investigation into binary and complex mixtures of disks with different D_r and Ω values, substituting D_r by D_r^i and Ω by Ω^i in eqn (2).

We note that the orientation dynamics in eqn (2) are decoupled from the position dynamics in eqn (1), and result from the interplay between deterministic chirality and angular diffusion. The deterministic angular speed Ω sets a rotational timescale $\tau_\Omega = \Omega^{-1}$; the diffusion constant D_r sets a persistence timescale $\tau_r = D_r^{-1}$. We will show below that the interplay between rotational, persistence, and elastic timescales can generate different collective states.

3 State space overview

We begin by characterizing the different regimes that can be reached by the model introduced above. Fig. 1(a) presents a diagram of the resulting phases as a function of the chiral angular speed Ω and the angular diffusion coefficient D_r, with the boundaries computed analytically as we will detail in Section 4. Broadly speaking, the system develops mesoscopic range order for low enough Ω and D_r values (below the blue line), where patches of disks with strong velocity correlations spontaneously appear at different scales. For high Ω/D_r ratios (above the red line) the velocity directions displayed by these patches rotate with a clearly defined chirality, determined by Ω, defining the chiral mesoscopic range order (CMRO) regime. For low Ω/D_r ratios, no clear chirality is observed and we define the mesoscopic range order (MRO) regime. In the high Ω and high D_r regimes (beyond the blue line), we find instead no extended regions of high velocity correlation. The individual particle motion is dominated by deterministic chiral rotation for high Ω/D_r ratios (above the red line), in the chiral disorder (CD) regime, and by stochastic rotational diffusion for low Ω/D_r ratios (below the red line), in the dynamic disorder (DD) regime. Note that the transitions between the four regimes are smooth and determined by the spatiotemporal dynamics.

Fig. 1(b) and (c) present snapshots of the velocity vectors and kymographs, respectively, describing the spatiotemporal dynamics of the velocity angles, for simulations in each one of the four regimes. Here the sub-panels correspond to: (i) the MRO regime for $D_r = 10^{-2}$, $\Omega = 10^{-3}$, see ESI,† (ref. 92) Movie S1;[92] (ii) the CMRO regime for $D_r = 10^{-3}$, $\Omega = 10^{-2}$, see Movie S2 (ESI†);[92] (iii) the DD regime for $D_r = 5$, $\Omega = 10^{-2}$, see Movie S3 (ESI†);[92] and (iv) the CD regime for $D_r = 10^{-2}$, $\Omega = 5$, see Movie S4 (ESI†).[92]

All simulations were carried out for $N = 3183$ disks of radius $r_0 = 1$ in a periodic square box of side $L = 100$, which results in a packing fraction of $\phi = N\pi r_0^2/L^2 \approx 1$, and for the following simulation parameters (unless otherwise stated): mobility $\mu = 1$, elastic repulsive strength $k = 1$, and active speed $v_0 = 0.01$. The simulations were performed at sufficiently high density and low active speed to avoid melting, phase separation, and clustering, in order to focus on the linear response regime. Spatially, the disks form a crystalline triangular packings without defects, well in the solid phase, without rearrangements for the

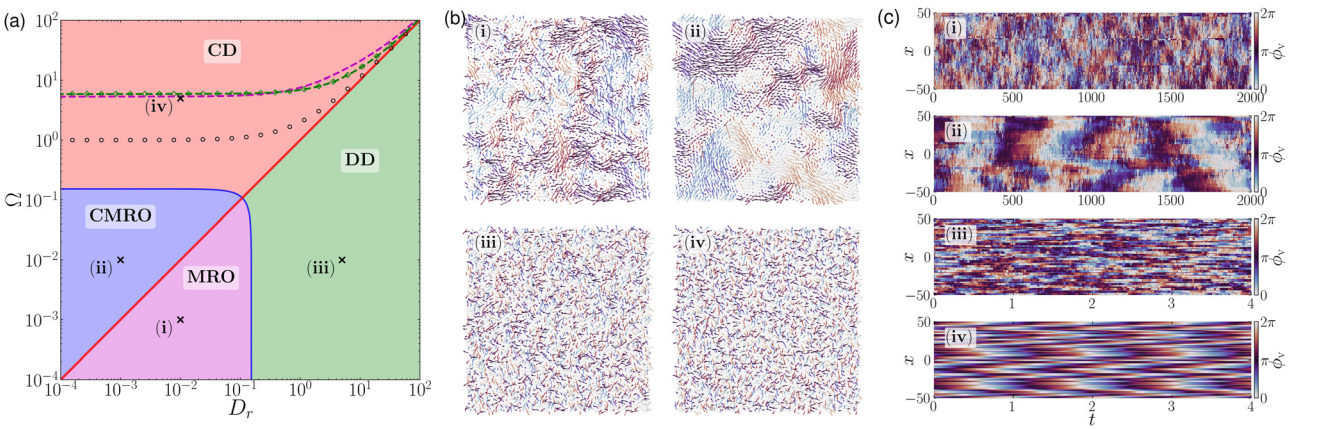

Fig. 1 Dynamical regimes and collective states identified in an active solid with noisy chiral dynamics. (a) Phases on the $D_r - \Omega$ plane: mesoscopic range order (MRO), chiral mesoscopic range order (CMRO), dynamic disorder (DD), and chiral disorder (CD). The red line traces $D_r = \Omega$, separating the chiral ($D_r < \Omega$) and achiral ($D_r \geq \Omega$) regimes. The blue line represents $\xi_T = l_0$, where l_0 is the equilibrium distance between neighboring particles. The dashed green line and open green diamonds trace two analytical approximations of the maxima of the elastic energy. The magenta dashed line shows an analytical expression for the minima of the mean-squared velocity, and thus also of the kinetic energy. The black open circles curve provides the analytical result for the maximum of the steady-state mean-squared displacement of a single particle in a harmonic well (see Appendix B). (b) Snapshots of simulations in the four regimes: (i) MRO, (ii) CMRO, (iii) DD, and (iv) CD. Each arrow is colored by angle and represents the direction and magnitude of the velocity vector of the disc at its location. (c) Kymographs corresponding to the snapshots, depicting space-time plots of the velocity angles obtained from simulations, following the dynamics in time of a slice of the system along the x direction. The snapshots and kymographs display results of simulations performed with the parameter combinations indicated by crosses in the phase diagram in panel (a).

duration of the simulation. In the snapshots, each disk is represented by a small arrow starting at $\mathbf{r}_i$, pointing towards $\dot{\mathbf{r}}_i$, with length proportional to $\|\dot{\mathbf{r}}_i\|$, and colored by angle. In the kymographs, we use colors to display the angle of the velocity $\dot{\mathbf{r}}_i$ of all disks located within a narrow slit, with $-r_0 \leq y \leq +r_0$, as a function of their x position and time.

The snapshots in sub-panels (i) and (ii) of Fig. 1(b) clearly show the emergence of mesoscopic-range order, while the kymographs in sub-panels (i) and (ii) of Fig. 1(c) show that their temporal dynamics is distinct, with only sub-panel (ii) showing periodic dynamics that result from a close to deterministic local rotation of the $\hat{n}_i$ vector. Correspondingly, the snapshots in sub-panels (iii) and (iv) of Fig. 1(b) show disordered states, while the kymographs in sub-panels (iii) and (iv) of Fig. 1(c) show that the dynamics in the DD regime is random in time while the CD regime dynamics is quasiperiodic. Note that the periodicity of the angular dynamics in sub-panels (ii) and (iv) of Fig. 1(c) matches the expected full rotation period $T = 2\pi/\Omega$, with $T = 200\pi \simeq 628.32$ for (ii) and $T = 2\pi/5 \simeq 1.26$ for (iv).

In addition to the four regimes described above, the diagram in Fig. 1(a) also contains dashed green and magenta lines, as well as lines of open black circles and green diamonds. These trace four different analytical approximations for the location in the diagram of the 'hammering state' identified in ref. 89, where the elastic energy contained by the system is maximal and its kinetic energy is minimal (see ESI,† (ref. 92) Movie S5[92] for a simulation with $D_r = \Omega = 10$).

We will deduce analytically below the dynamics and boundaries of the different regimes described above.

4 Analytical results

In this section, we present the analytical formulations used to describe the system. We begin by computing the orientation dynamics of the heading direction in Section A, since they are not coupled to the positions. We then formulate a linear response theory, adopting the method in Henkes *et al.*[93] to describe the linear response in terms of normal modes in Section B, to then calculate the energy per mode and spatial velocity correlations. We further simplify the analytical description by implementing a continuum elasticity framework in Section C, to compute mean-squared velocity and velocity autocorrelation functions.

4.1 Orientation dynamics

Given that the orientation evolves independently in eqn (2), the probability distribution $P(\hat{n},t)$ for the heading direction $\hat{n}$ as a function of time will follow the Fokker–Planck equation

$$\partial_t P(\hat{n},t) = D_r \nabla_{\hat{n}}{}^2 P - \Omega \hat{n}^{\perp} \cdot \nabla_{\hat{n}} P, \tag{3}$$

where $\nabla_{\hat{n}}$ is the Laplacian in orientation space. Using a Laplace transformation approach described in detail in Appendix A, we can compute an exact expression for the heading orientation autocorrelation, which is given by

$$\langle \hat{n}(t) \cdot \hat{n}(0) \rangle = e^{-D_r t} \cos(\Omega t). \tag{4}$$

Here, the decay rate of the exponential term is given by $\tau_r = {D_r}^{-1}$ and the period of chiral rotation, by $\tau_\Omega = \Omega^{-1}$. We thus define $D_r = \Omega$ as the critical line between a regime dominated by the angular noise and a regime dominated by the deterministic chirality, which we highlighted as the red diagonal line in Fig. 1(a). Note that this boundary is formally analogous in eqn (4) to the limit between damped and overdamped oscillations, where the high angular diffusion case corresponds to the overdamped regime, as the mean temporal heading correlations display no oscillatory component.

4.2 Normal mode formulation

In order to express the dynamics in terms of the normal modes of vibration of the passive system, we first define as $\mathbf{r}_i^0$ the equilibrium position of disk i for $v_0 = 0$, which corresponds to a minimum of the elastic energy. Using eqn (1), we then find that the dynamics of small displacements $\delta\mathbf{r}_i = \mathbf{r}_i - \mathbf{r}_i^0$ around these equilibrium positions are described by

$$\delta\dot{\mathbf{r}}_i = v_0 \hat{n}_i - \sum_j \mathbb{K}_{ij} \cdot \delta\mathbf{r}_j, \tag{5}$$

where each $\mathbb{K}_{ij}$ corresponds to a 2×2 block of the $2N \times 2N$ dynamical matrix. We are interested in expressing the dynamics over the normal elastic modes of the system, *i.e.*, over the eigenvectors of the dynamical matrix. Each of these $2N$ normal modes corresponds to a $2N$-dimensional eigenvector that can be written as a list of N two-dimensional vectors, given by $(\xi_1^\nu, \ldots, \xi_N^\nu)$, where $\nu = 1, \ldots, 2N$ labels the eigenvector mode associated to the eigenvalue λ_ν.

We can formally write the displacements in terms of the eigenmodes described above as $\delta\mathbf{r}_i = \sum_{\nu=1}^{2N} a_\nu \xi_i^\nu$. Projecting eqn (5) onto the normal modes, we then obtain the following uncoupled equations for the dynamics of the normal mode amplitudes:

$$\dot{a}_\nu = \eta_\nu - \lambda_\nu a_\nu, \tag{6}$$

where η_ν is the projection of the self-propulsion force onto the normal mode ν, given by

$$\eta_\nu = v_0 \sum_{i=1}^{N} \hat{n}_i \cdot \xi_i^\nu. \tag{7}$$

We note that η_ν is the sum of N statistically independent contributions with bounded moments, each one resulting from the correlated noise dynamics in time that is followed by its corresponding $\hat{n}_i$. The central limit theorem then implies that η_ν must follow a Gaussian distribution, here with $\langle \eta_\nu(t) \rangle = 0$. Additionally, since the eigenvectors form an orthonormal basis where $\sum_{i=1}^{N} \xi_i^\nu \cdot \xi_i^{\nu'} = \delta_{\nu,\nu'}$, the corresponding two-time correlation function will be given by $\langle \eta_\nu(t) \eta_{\nu'}(t') \rangle = ({v_0}^2/2) \langle \hat{n}(t) \cdot \hat{n}(t') \rangle \delta_{\nu,\nu'}$. Replacing the heading autocorrelation expression in eqn (4), we finally obtain $\langle \eta_\nu(t) \eta_\nu(0) \rangle = ({v_0}^2/2) e^{-D_r t} \cos(\Omega t)$, which implies that the statistical properties of the noise η_ν are the same for any mode ν.

We now calculate the mean potential energy stored in each mode (see ESI,† (ref. 92) Section SII for details). By solving eqn (6), we first find

$$a_\nu(t) = a_\nu(0)e^{-\lambda_\nu t} + \int_0^t \mathrm{d}t' \eta_\nu(t') e^{-\lambda_\nu (t-t')}. \tag{8}$$

From here, we can obtain the steady state mean squared value of $a_\nu(t)$ by computing $\lim_{t\to\infty}\langle a_\nu^2(t)\rangle$ to obtain

$$\langle a_\nu^2\rangle = \frac{v_0^2(D_\mathrm{r}+\lambda_\nu)}{2\lambda_\nu\left[(D_\mathrm{r}+\lambda_\nu)^2+\Omega^2\right]}. \tag{9}$$

The mean energy per mode is given by $E_\nu = \lambda_\nu\langle a_\nu^2\rangle/2$ and can thus be expressed as

$$E_\nu = \frac{v_0^2(D_\mathrm{r}+\lambda_\nu)}{4\left[(D_\mathrm{r}+\lambda_\nu)^2+\Omega^2\right]}. \tag{10}$$

We note in this equation that there is a critical curve in the $D_\mathrm{r}-\Omega$ plane that maximizes the mean potential energy injected into the system by the combined activity of all modes (as shown in Fig. S2 of the ESI,† (ref. 92)). We can obtain an approximate expression for this curve by finding the conditions that maximize the energy of the stiffest mode only (*i.e.*, the mode least excited by the activity), which we identified as the main responsible for the maximum in the total potential energy. Since the stiffest mode corresponds to the largest eigenvalue $\lambda_\nu = \lambda_\mathrm{max}$, its energy will be $E^* = E_\nu|_{\lambda_\nu=\lambda_\mathrm{max}}$ and its maximum can be computed using $\partial E^*/\partial D_\mathrm{r} = 0$. We thus find that the potential energy injected by activity is approximately maximized for $D_\mathrm{r}^* = \Omega - \lambda_\mathrm{max}$, corresponding to the dominant mode, *i.e.* the maximum eigenvalue $\lambda_\mathrm{max} = 5.93 \pm 0.01$. This curve is displayed as the open green diamonds in Fig. 1(a).

In Fig. 2(c), we visualize a color map of the energy $E/Nv_0^2 = \sum_\nu E_\nu/Nv_0^2$ on the $D_\mathrm{r}-\Omega$ plane that clearly shows an increase of elastic energy in the low D_r and low Ω regimes. Fig. 2(e) presents E/Nv_0^2 as function of D_r for three different $\Omega = 1, 10, 20$ values, showing the presence of a maximum at intermediate D_r noise strengths, for high chirality ($\Omega = 10, 20$). In this regime, we thus find that the elastic energy can grow despite an increase in noise strength. In Fig. 2(g), we plot E/Nv_0^2 as function of Ω for three different $D_\mathrm{r} = 1, 10, 20$ values, showing a monotonic decrease of the elastic energy. We display the maximum of E/Nv_0^2 in the $D_\mathrm{r}-\Omega$ plane as the dashed green line in Fig. 1(a), which matches the previously computed $D_\mathrm{r}^* = \Omega - \lambda_\mathrm{max}$ curve. This curve suggests that an increase in elastic energy with noise strength indicates the presence of the 'hammering state'.[89]

Eqn (10) also provides us with expressions for the low and high limits of angular noise or chirality. In the high noise case, $D_\mathrm{r}/\lambda_\nu \gg 1$ and the mean energy per mode reduces to $E_\nu \approx v_0^2 D_\mathrm{r}/4(D_\mathrm{r}^2+\Omega^2)$, which gives rise to two limits: (i) a low chirality limit $\Omega \to 0$, where $E_\nu \to v_0^2/4D_\mathrm{r}$, and (ii) a high chirality limit $\Omega \to \infty$, where $E_\nu \to 0$. This latter limit is connected to the fact that very high chirality disrupts the persistent translation driven by self-propulsion. In a chiral crystal with infinite chirality, particles turn in place and displacements behave like in a zero-temperature system, which also suppresses wall accumulation[94] and MIPS.[41] In the low noise case $D_\mathrm{r} \to 0$, we find $E_\nu = v_0^2/4[\lambda_\nu^2+\Omega^2]$, which also gives rise to two limits: (i) a low chirality limit with $E_\nu \to v_0^2/4\lambda_\nu^2$, where the lowest modes with $\lambda_\nu \ll 1$ are enhanced, and (ii) a high chirality limit with $E_\nu \to v_0^2/4\Omega^2$. On the other hand, for any noise value, in the $\Omega \to 0$ limit, we recover from eqn (10) the same expressions previously obtained in ref. 70 and 93 for standard (non-chiral or achiral) active particles, as expected.

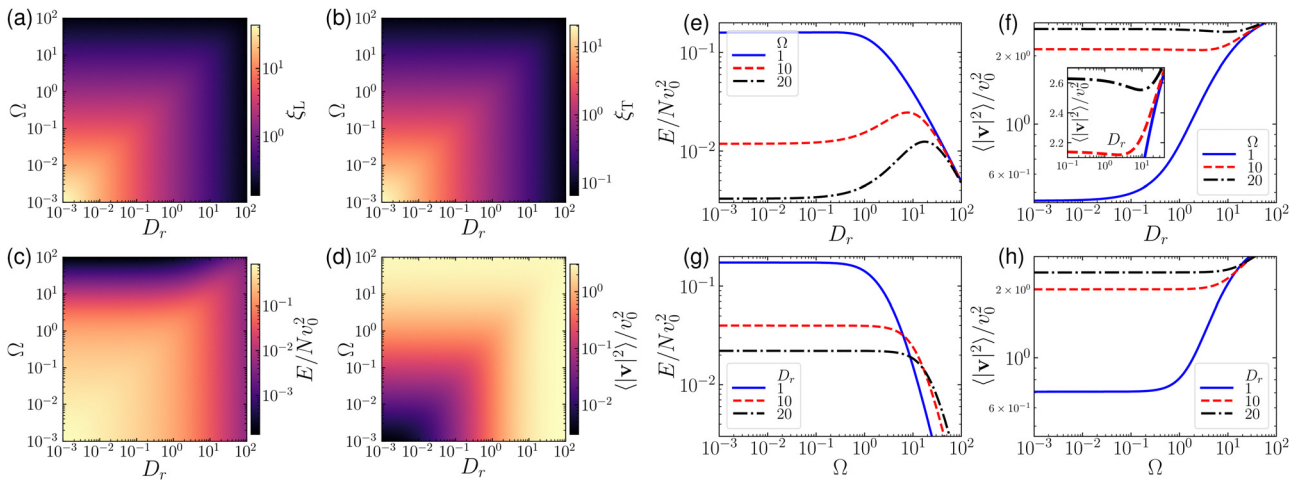

Fig. 2 Analytical features of the characteristic length scales, energy, and mean-squared velocity in an active solid with noisy chiral dynamics. (a) and (b) Color maps of the longitudinal ξ_L and transverse ξ_T characteristic length scales on the $D_\mathrm{r}-\Omega$ plane, respectively, computed using the continuum elastic formulation in eqn (19). (c) Color map of the energy $E/Nv_0^2 = \sum E_\nu/Nv_0^2$ on the $D_\mathrm{r}-\Omega$ plane, as derived from the normal mode formulation in eqn (10). (d) Color map of the mean-squared velocity $\langle|\mathbf{v}|^2\rangle/v_0^2$ on the $D_\mathrm{r}^\nu-\Omega$ plane, resulting from the continuum elastic formulation in eqn (20). (e) and (f) Plot of E/Nv_0^2 and of $\langle|\mathbf{v}|^2\rangle/v_0^2$, respectively, as a function of D_r, for $\Omega = 1, 10, 20$. The inset zooms into the minimum of $\langle|\mathbf{v}|^2\rangle/v_0^2$ that appears at high Ω values. (g) and (h) Plot of E/Nv_0^2 and of $\langle|\mathbf{v}|^2\rangle/v_0^2$, respectively, as a function of Ω, for $D_\mathrm{r} = 1, 10, 20$.

Finally, in order to identify the emergence of mesoscopic order, we are interested in finding the mean velocity spectrum (see ESI,† (ref. 92) Section SIIA for details). We begin by expressing the velocity in Fourier space, computing its discrete Fourier transform $\mathbf{v}(\mathbf{q}) = \sum_{j=1}^{N} e^{i\mathbf{q}\cdot\mathbf{r}_j^0}\delta\dot{\mathbf{r}}_j/N$ in terms of the $\mathbf{r}_i^0$ equilibrium reference positions of the disks. Expanding $\delta\dot{\mathbf{r}}_j$ in the normal mode basis, we find

$$\begin{aligned}\left\langle\left|\mathbf{v}(\mathbf{q})^2\right|\right\rangle &= \langle\mathbf{v}(\mathbf{q})\cdot\mathbf{v}^*(\mathbf{q})\rangle = \sum_{\nu,\nu'}\langle\dot{a}_\nu\dot{a}_{\nu'}\rangle\xi_\nu(\mathbf{q})\cdot\xi^*_{\nu'}(\mathbf{q})\\ &= \sum_{\nu,\nu'}\langle\dot{a}_\nu{}^2\rangle|\xi_\nu(\mathbf{q})|^2\delta_{\nu\nu'},\end{aligned} \tag{11}$$

where we defined $\xi_\nu(\mathbf{q}) = \sum_{j=1}^{N} e^{i\mathbf{q}\cdot\mathbf{r}_j^0}\xi_j^\nu\Big/N$ as the discrete Fourier transform of the eigenvectors. Using eqn (6), we then replace $\langle\dot{a}_\nu{}^2\rangle = \lambda_\nu{}^2\langle a_\nu{}^2\rangle - 2\lambda_\nu\langle a_\nu\eta_\nu\rangle + \langle\eta_\nu{}^2\rangle$ into eqn (11). Here, the $\langle a_\nu{}^2\rangle$ term is known from eqn (9), the equal-time correlation $\langle\eta_\nu{}^2\rangle = v_0{}^2/2$ can be computed from eqn (7), and the expression for $\langle a_\nu\eta_\nu\rangle = v_0{}^2(D_\mathrm{r}+\lambda_\nu)/2[(D_\mathrm{r}+\lambda_\nu)^2+\Omega^2]$ in the steady-state ($t\to\infty$) can be obtained from eqn (8). This leads to the following explicit expression for the velocity correlation function:

$$\left\langle\left|\mathbf{v}(\mathbf{q})^2\right|\right\rangle = \frac{v_0{}^2}{2}\sum_\nu\left[1-\frac{\lambda_\nu(D_\mathrm{r}+\lambda_\nu)}{(D_\mathrm{r}+\lambda_\nu)^2+\Omega^2}\right]|\xi_\nu(\mathbf{q})|^2. \tag{12}$$

This equation allows us examine different limits. For $\Omega = 0$, it simplifies to the velocity correlation function $\left\langle\left|\mathbf{v}(\mathbf{q})^2\right|\right\rangle = \left(v_0{}^2/2\right)\sum_\nu[D_\mathrm{r}/(D_\mathrm{r}+\lambda_\nu)]|\xi_\nu(\mathbf{q})|^2$, previously obtained for achiral active particles in ref. 93. For $D_\mathrm{r} = 0$, it simplifies to the velocity correlation function $\left\langle\left|\mathbf{v}(\mathbf{q})^2\right|\right\rangle = \left(v_0{}^2/2\right)\sum_\nu\left[\Omega^2/\left(\Omega^2+\lambda_\nu{}^2\right)\right]|\xi_\nu(\mathbf{q})|^2$ for disordered deterministic rotators.

In most experimental contexts, the extraction of the normal modes or their eigenvalues is unfeasible, except in specific scenarios like colloidal particle experiments.[95–97] Current methods are often restricted to measuring in thermal equilibrium conditions and necessitate extensive data gathering. In the next subsection, we will therefore extend our findings to the framework of continuum elasticity theory, which only requires knowing the elastic constants of the material and is thus much easier to compute for real-world systems.

4.3 Continuum elastic formulation

To derive the continuum formulation, we begin by writing the equation of motion for the displacement vector field $\mathbf{u}(\mathbf{r}) = \mathbf{r}'(\mathbf{r}) - \mathbf{r}$, which describes the deformed state $\mathbf{r}'(\mathbf{r})$ with respect to the equilibrium reference state $\mathbf{r}$. As detailed in the ESI,† (ref. 92) in the presence of active forces this equation is given by

$$\dot{\mathbf{u}} = \nabla\cdot\sigma + \mathbf{f}_\mathrm{act}. \tag{13}$$

Here, σ is the passive stress tensor, with components $\sigma_{\alpha\beta} = B\delta_{\alpha\beta}u_{\gamma\gamma} + 2G\left(u_{\alpha\beta} - \frac{1}{2}\delta_{\alpha\beta}u_{\gamma\gamma}\right)$, and activity is introduced through self-propulsion forces defined by $\mathbf{f}_\mathrm{act}(\mathbf{r},t) = v_0\hat{n}(\mathbf{r},t)$. In this expression for the stress tensor, B and G correspond respectively to the bulk and shear moduli of the isotropic solid, the strain tensor components $u_{\alpha\beta} = \frac{1}{2}\left[\partial_\alpha u_\beta + \partial_\beta u_\alpha\right]$ are written in terms of spatial derivatives of the displacement vectors $\mathbf{u}(\mathbf{r})$ with respect to $\alpha,\beta \in \{x,y\}$, and the summation over repeated indexes is assumed. We can see explicitly in eqn (13) that this active solid is distinct from odd active matter, which only considers internal active stresses that can be written in terms of effective moduli.[58]

To proceed with the computations, we define the direct and inverse spatiotemporal Fourier transforms as

$$\mathbf{u}(\mathbf{r},t) = \frac{1}{(2\pi)^3}\int\mathrm{d}^2\mathbf{q}\int\mathrm{d}\omega\tilde{\mathbf{u}}(\mathbf{q},\omega)e^{-i(\mathbf{q}\cdot\mathbf{r}+\omega t)},$$

$$\tilde{\mathbf{u}}(\mathbf{q},\omega) = \int\mathrm{d}^2\mathbf{r}\int\mathrm{d}t\mathbf{u}(\mathbf{r},t)e^{i(\mathbf{q}\cdot\mathbf{r}+\omega t)},$$

and write the continuum equation of motion (13) in Fourier space as

$$-i\omega\tilde{\mathbf{u}}(\mathbf{q},\omega) = \tilde{\mathbf{f}}_\mathrm{act}(\mathbf{q},\omega) - \mathbb{D}(\mathbf{q})\tilde{\mathbf{u}}(\mathbf{q},\omega). \tag{14}$$

Here, $\mathbb{D}(\mathbf{q})$ is a 2×2 dynamic matrix in Fourier space, given by

$$\mathbb{D}(\mathbf{q}) = \begin{bmatrix} Bq_x{}^2 + Gq^2 & Bq_xq_y \\ Bq_xq_y & Bq_y{}^2 + Gq^2\end{bmatrix},$$

where $q^2 = q_x{}^2 + q_y{}^2$ (see ESI,† (ref. 92) for a detailed derivation), and we defined the active force $\mathbf{f}_\mathrm{act}(\mathbf{r},t)$ in Fourier space as

$$\tilde{\mathbf{f}}_\mathrm{act}(\mathbf{q},\omega) = v_0\int\mathrm{d}^2\mathbf{r}\int_{-\infty}^{\infty}\mathrm{d}t\hat{n}(\mathbf{r},t)e^{i(\mathbf{q}\cdot\mathbf{r}+\omega t)}. \tag{15}$$

We are interested in computing the velocity correlation functions. To do this, we begin by writing the orientational correlation in the continuum limit, replacing $\hat{n}_i(t)$ by a continuous field $\hat{n}(\mathbf{r},t)$, with $\langle\hat{n}_i(t)\cdot\hat{n}_j(t')\rangle = \delta_{i,j}\langle\hat{n}(t)\cdot\hat{n}(t')\rangle$. We then substitute the Kronecker delta $\delta_{i,j}$ by its Dirac counterpart, using $\delta_{i,j}\to a^2\delta(\mathbf{r}-\mathbf{r}')$, where a is the smallest characteristic length scale of the system, to obtain $\langle\hat{n}(\mathbf{r},t)\cdot\hat{n}(\mathbf{r}',t')\rangle = a^2\delta(\mathbf{r}-\mathbf{r}')\langle\hat{n}(t)\cdot\hat{n}(t')\rangle$. From eqn (15), it is then clear that $\langle\tilde{\mathbf{f}}_\mathrm{act}(\mathbf{q},\omega)\rangle = 0$, and the second order correlation function $C_{\tilde{\mathrm{F}}} = \langle\tilde{\mathbf{f}}_\mathrm{act}(\mathbf{q},\omega)\cdot\tilde{\mathbf{f}}_\mathrm{act}(\mathbf{q}',\omega')\rangle$ is simply given by

$$C_{\tilde{\mathrm{F}}} = \frac{2(2\pi)^3a^2v_0{}^2D_\mathrm{r}}{(\omega-\Omega)^2+D_\mathrm{r}{}^2}\delta(\mathbf{q}+\mathbf{q}')\delta(\omega+\omega'). \tag{16}$$

If we now consider a finite system (a square of side L, for simplicity), the wave vector becomes discretized. We can thus replace the Dirac delta by the Kronecker delta, $\delta(\mathbf{q}+\mathbf{q}')\to\frac{1}{(\Delta q)^2}\delta_{\mathbf{q}',-\mathbf{q}}$, with $\Delta q \equiv 2\pi/L$. This also leads us to define the spatially discrete Fourier transform $\mathbf{f}_\mathrm{act}(\mathbf{q},\omega) = \tilde{\mathbf{f}}_\mathrm{act}(\mathbf{q},\omega)/a^2$ for discrete spatial wave vectors $\mathbf{q}$ but continuous frequency ω. The correlation function for this discrete Fourier transform, given by $C_\mathrm{F} = \langle\mathbf{f}_\mathrm{act}(\mathbf{q},\omega)\cdot\mathbf{f}_\mathrm{act}(\mathbf{q}',\omega')\rangle$, will be equal to

$$C_\mathrm{F} = \frac{N\pi^2v_0{}^2D_\mathrm{r}}{\phi[(\omega-\Omega)^2+D_\mathrm{r}{}^2]}\delta(\omega+\omega'). \tag{17}$$

Finally, by decomposing eqn (15) into a its longitudinal and transverse components $\tilde{\mathbf{u}} = \tilde{u}_L(\mathbf{q},\omega)\hat{\mathbf{q}} + \tilde{u}_T(\mathbf{q},\omega)\hat{\mathbf{q}}_\perp$, with respect to the wave vector $\mathbf{q}$, we can use $\tilde{\mathbf{v}}(\mathbf{q},\omega) = -i\omega\tilde{\mathbf{u}}(\mathbf{q},\omega)$ to obtain the following expression for the mean-squared velocity in Fourier space

$$\langle|\mathbf{v}(\mathbf{q})|^2\rangle = \frac{Nv_0^2}{2}\left[\frac{1+\chi(\xi_L q)^2}{1+2\chi(\xi_L q)^2+(\xi_L q)^4} + \frac{1+\chi(\xi_T q)^2}{1+2\chi(\xi_T q)^2+(\xi_T q)^4}\right]. \tag{18}$$

Here, we have respectively defined the longitudinal and transverse characteristic length scales as

$$\xi_L = \sqrt{\frac{B+G}{\sqrt{D_r^2+\Omega^2}}},\ \xi_T = \sqrt{\frac{G}{\sqrt{D_r^2+\Omega^2}}}, \tag{19}$$

and the control parameter as $\chi = D_r/\sqrt{D_r^2+\Omega^2}$.

Fig. 2(a) and (b) display how the longitudinal and transverse characteristic length scales described by eqn (19) change across the different regimes on the $D_r - \Omega$ plane. In Fig. 1(a), we used these equations to define the blue line as the D_r and Ω values for which the smallest characteristic length scale ξ_T is equal to the typical equilibrium distance between particles l_0. Below this line, the system therefore develops mesoscopic scale correlations.

Next, we proceed to compute the mean-squared velocity $\langle|\mathbf{v}|^2\rangle$ of our system in real space. We can directly write the mean-squared velocity of all particles, $\langle|\mathbf{v}|^2\rangle = \left\langle\sum_i|\mathbf{v}_i|^2\right\rangle/N$, in continuum form as $\langle|\mathbf{v}|^2\rangle = [a^2/N(2\pi)^2]\int d^2\mathbf{q}\langle|\mathbf{v}(\mathbf{q})|^2\rangle$, where $\langle|\mathbf{v}(\mathbf{q})|^2\rangle$ is given by eqn (18). The upper limit of this integral is set by the inverse particle size, *i.e.*, by the maximum wave number $q_{max} = 2\pi/a$, where a is of the order of the particle size l_0. Using $\int d^2q = 2\pi\int q dq$, we can thus write

$$\langle|\mathbf{v}|^2\rangle = \frac{a^2}{2\pi N}\int dq q\langle|\mathbf{v}(\mathbf{q})|^2\rangle. \tag{20}$$

This expression can then be integrated numerically to compute the mean-squared velocity. In Fig. 2(d), we map $\langle|\mathbf{v}|^2\rangle/{v_0}^2$ on the $D_r - \Omega$ plane, showing that the mean-squared velocity is small for low D_r and low Ω values, in regimes displaying coherent mesoscopic motion.

Fig. 2(f) presents $\langle|\mathbf{v}|^2\rangle/{v_0}^2$ as function of D_r for three different values of Ω = 1, 10, 20. The figure inset shows that $\langle|\mathbf{v}|^2\rangle/{v_0}^2$ displays a minimum at intermediate noise strength D_r and high chirality (Ω = 10, 20). This implies that, as this minimum is reached, kinetic energy must be suppressed despite an increase in noise strength. Fig. 2(h) plots $\langle|\mathbf{v}|^2\rangle/{v_0}^2$ as function of Ω for three different values of D_r = 1, 10, 20. In Fig. 1(a), we defined the magenta dashed line as the minimum of the normalized mean-squared velocity $|\langle\mathbf{v}^2\rangle|/{v_0}^2$, where most of the self-propulsion forces feed into the potential energy. This curve can be directly computed through a numerical integration of eqn (20).

Finally, we will now use the continuum formulation to investigate the collective temporal dynamics of the system (see ESI,† (ref. 92) Sections SIIIB-C for details). First, we directly calculate the velocity autocorrelation function as the integral over Fourier space

$$\langle\mathbf{v}(t)\cdot\mathbf{v}(t')\rangle = \frac{1}{(2\pi)^4}\int d^2\mathbf{q}\int d^2\mathbf{q}'\langle\tilde{\mathbf{v}}(\mathbf{q},t)\cdot\tilde{\mathbf{v}}(\mathbf{q}',t')\rangle. \tag{21}$$

Here, $\langle\tilde{\mathbf{v}}(\mathbf{q},t)\cdot\tilde{\mathbf{v}}(\mathbf{q}',t')\rangle$ can be written in terms of the Fourier integral of $\langle\tilde{\mathbf{v}}(\mathbf{q},\omega)\cdot\tilde{\mathbf{v}}(\mathbf{q}',\omega')\rangle$ over the frequencies ω and ω'. A long yet straightforward calculation then leads to the following expression for the velocity autocorrelation function

$$\begin{aligned}\langle\mathbf{v}(t)\cdot\mathbf{v}(0)\rangle = \frac{a^2v_0^2}{4\pi}\int_{q_{min}}^{q_{max}} dq q\times\Bigg[&\frac{\left[\left[(B+G)^2q^4\left(\Omega^2-D_r^2\right)+\left(\Omega^2+D_r^2\right)^2\right]\cos(\Omega t)-2\Omega D_r(B+G)^2q^4\sin(\Omega t)\right]e^{-D_r t}}{\left[((B+G)^2q^4+\Omega^2-D_r^2)^2+4D_r^2\Omega^2\right]}\\ &+\frac{\left[\left[G^2q^4\left(\Omega^2-D_r^2\right)+\left(\Omega^2+D_r^2\right)^2\right]\cos(\Omega t)-2\Omega D_r G^2q^4\sin(\Omega t)\right]e^{-D_r t}}{\left[(G^2q^4+\Omega^2-D_r^2)^2+4D_r^2\Omega^2\right]}\\ &-\frac{(B+G)q^2D_r\left(D_r^2+\Omega^2-(B+G)^2q^4\right)e^{-(B+G)q^2t}}{\left[\left(D_r^2+\Omega^2-(B+G)^2q^4\right)^2+4(B+G)^2q^4\Omega^2\right]}-\frac{Gq^2D_r\left(D_r^2+\Omega^2-G^2q^4\right)e^{-Gq^2t}}{\left[\left(D_r^2+\Omega^2-G^2q^4\right)^2+4G^2q^4\Omega^2\right]}\Bigg].\end{aligned} \tag{22}$$

We note that the integral above must be computed numerically and that the integration limits, q_{min} and q_{max}, are respectively determined by the largest and smallest scales of the system. Fig. S3 in the ESI,† (ref. 92) illustrates eqn (22) in the no chirality limit Ω = 0 (panel a), in the noiseless limit D_r = 0 (panel b), for fixed Ω as a function of D_r (panel c), and for a fixed D_r as a function of Ω (panel d). Oscillations with frequency Ω appear in all cases where $\Omega > D_r$.

We finalize this section by exploring the scaling of the mean-squared velocity in eqn (18) in two limiting cases: the achiral active limit for χ = 1 (setting Ω = 0) and the limit with no noise χ = 0 (setting D_r = 0). In the achiral active case, $\langle|\mathbf{v}(\mathbf{q})|^2\rangle$ scales as $\sim(\xi_T q)^{-2}$ and in the no noise case, it scales as $\langle|\mathbf{v}(\mathbf{q})|^2\rangle \sim (\xi_T q)^{-4}$. In both limiting cases, $\langle|\mathbf{v}(\mathbf{q})|^2\rangle$ thus diverges for vanishing q, but with a different scaling.

In these two limiting cases, we can also compute the closed-form analytic mean-squared velocity. In the achiral active limit (Ω = 0), we get the previously obtained result[93]

$$\langle|\mathbf{v}|^2\rangle = \frac{a^2v_0^2}{8\pi}\left[\frac{\log\left(1+{\xi_L}^2{q_{max}}^2\right)}{{\xi_L}^2}+\frac{\log\left(1+{\xi_T}^2{q_{max}}^2\right)}{{\xi_T}^2}\right].$$

This expression shows that the dominant scaling, $\langle|\mathbf{v}|^2\rangle \sim \xi_T^{-2}$ or $\langle|\mathbf{v}|^2\rangle \sim \xi_L^{-2}$, will follow the scaling Ansatz used for highly dense collective cellular motion in a monolayer.[98] In the limit of no noise ($D_r = 0$), we find

$$\langle|\mathbf{v}|^2\rangle = \frac{a^2 v_0^2}{8\pi}\left[\frac{\tan^{-1}\left(\xi_L^2 q_{max}^2\right)}{\xi_L^2} + \frac{\tan^{-1}\left(\xi_T^2 q_{max}^2\right)}{\xi_T^2}\right],$$

which also shows the dominant scaling $\langle|\mathbf{v}|^2\rangle \sim \xi_T^{-2}$ or $\langle|\mathbf{v}|^2\rangle \sim \xi_L^{-2}$. Note that the mean-squared velocity will have small values in regimes of low chirality and low noise, which matches the regime where elastic energy is stored in the sheet, leading to the emergence of the mesoscopic correlated motion in the velocity fields.

5 Comparison with simulations

To compare the analytical predictions developed in the previous section with simulations, we computed the spatial velocity correlations in Fourier space $\langle|\mathbf{v}(\mathbf{q})|^2\rangle$ as well as the velocity and orientation autocorrelation functions ($C_{\mathbf{vv}}(t) = \langle\mathbf{v}(t)\cdot\mathbf{v}(0)\rangle$ and $C_{\hat{n}\hat{n}}(t) = \langle\hat{n}(t)\cdot\hat{n}(0)\rangle$, respectively) for a broad range of values of D_r and Ω. We focus on the two most salient regimes identified above: the emergence of correlated velocity fields for small D_r and Ω values (Section 5.1), and the extrema of the elastic and kinetic energy at high D_r and Ω values (Section 5.2).

5.1 Chiral mesoscopic range order

Fig. 3(a) presents simulation snapshots of the velocity angles showing the emergence of a CMRO state displaying correlated velocity fields for small values of D_r and Ω, as shown in the analytically computed state space diagram in Fig. 1(a).

Fig. 3(b) and (d) present the spatial velocity correlations in Fourier space, $\langle|\mathbf{v}(\mathbf{q})^2|\rangle$ as a function of $|\mathbf{q}|$, for a range of D_r = 0.01, 0.1, 0.5, 1.0 values with fixed Ω = 0.1, and for a range of Ω = 0.01, 0.1, 0.5, 1.0 values with fixed D_r = 0.01, respectively. We observe excellent agreement between the analytical normal mode formulation in eqn (12) and the simulation results (respectively solid lines and symbols), showing the emergence of correlated velocity fields for small D_r and Ω. The continuum elastic formulation in eqn (18), displayed as dashed lines, also shows good agreement with the simulations at low q, as expected.

Fig. 3(c) and (e), show the temporal autocorrelation functions for the orientations and normalized velocities, labeled $C_{\hat{n}\hat{n}}(t)$ and $C_{\mathbf{vv}}(t)$, respectively. Here, the $C_{\hat{n}\hat{n}}$ analytical curves in eqn (4) are represented by dashed lines and their numerical values by open symbols, while the $C_{\mathbf{vv}}$ analytical curves (22) are displayed as solid lines and their numerical values as solid symbols. In order to best match the numerical integration in eqn (22) to our simulations, we chose q_{min} and q_{max} as the smallest and largest simulated scales, as detailed in Appendix C. The red curves and symbols in Fig. 3(c) and (e) show that both autocorrelation functions, $C_{\hat{n}\hat{n}}$ and $C_{\mathbf{vv}}$, display an oscillatory behavior for D_r = 0.01 and Ω = 0.1. The black curves and symbols show instead a non-oscillatory behavior for higher nose D_r = 0.1 in Fig. 3(c), and for lower chirality Ω = 0.01 in Fig. 3(e), presenting a faster decay in the $C_{\mathbf{vv}}$ case.

5.2 Elastic and kinetic energy extrema

We now compare our analytical and numerical results on the elastic and kinetic energy extrema found in the high noise D_r, high chirality Ω regime. First, we note that no such extrema is observed in active solids composed of achiral active particles,

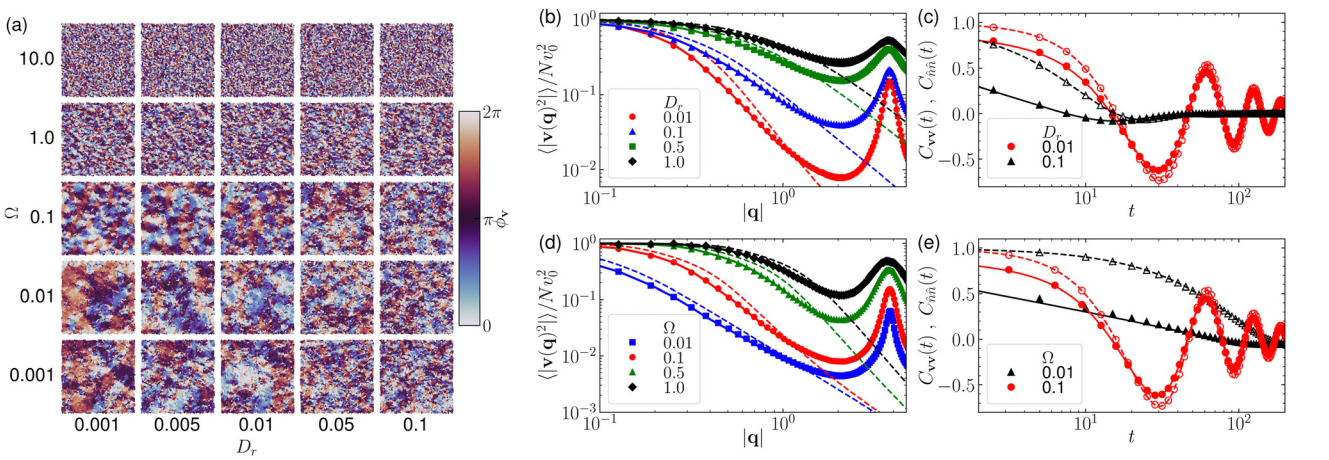

Fig. 3 Emergence of chiral mesoscopic range order at low chirality and low noise. (a) Snapshots in the $\Omega - D_r$ parameter space illustrating the emergent spatial correlations on the particle velocity angles $\phi_{\mathbf{v}} = \tan^{-1}(v_y/v_x)$. (b) and (d) Fourier space representation of the mean-squared velocity $\langle|\mathbf{v}(\mathbf{q})^2|\rangle/Nv_0^2$ as a function of $|\mathbf{q}|$, for different values of D_r with fixed Ω = 0.1, and for different values of Ω with fixed D_r = 0.01, respectively. Symbols represent simulations, solid lines result from the normal mode formulation in eqn (12), and dashed lines correspond to the continuum elastic approximation in eqn (18). (c) and (e) Normalized velocity autocorrelation functions $C_{\mathbf{vv}}(t) = \langle\mathbf{v}(t)\cdot\mathbf{v}(0)\rangle/\langle\mathbf{v}(0)^2\rangle$ (filled symbols and solid lines) and orientation autocorrelation functions $C_{\hat{n}\hat{n}}(t) = \langle\hat{n}(t)\cdot\hat{n}(0)\rangle$ (open symbols and dashed lines) as a function of time t, for for different values of D_r and fixed Ω = 0.1, and for different values of Ω and fixed D_r = 0.01, respectively. Symbols represent simulations again, solid lines display the $C_{\mathbf{vv}}(t)$ in eqn (22), resulting from the continuum elastic formulation, and dashed lines correspond to the orientation autocorrelation in eqn (4).

where the mean stored elastic energy always decreases with noise D_r. This also holds true for active solids composed of self-propelled particles with noisy chiral dynamics in the low chirality regime, with $\Omega < \lambda_{max}$, as it was shown in Fig. 1(a).

In the high chirality regime $\Omega > \lambda_{max}$, however, there is a range of D_r values for which the mean potential energy stored in all modes increases with D_r, as shown in Fig. 2(e). This leads to a maximum in the mean stored elastic energy as a function of D_r, shown by the dashed green line in Fig. 1(a). In the same regime, the mean-squared velocity obtained from the continuum elastic formulation displays non-monotonic behavior, leading to the minimum in the kinetic energy shown in Fig. 2(f), which was displayed as the magenta dashed line in Fig. 1(a).

The non-monotonic features described above are also captured by the case of a single particle in a harmonic trap, which results in the curve with open black circles in Fig. 1(a). This can be seen in the mean square displacement $\langle \mathbf{r}^2 \rangle(t)$ presented in Fig. 4(a), the $C_{\mathbf{vv}}(t)$ in Fig. 4(b), and the $\langle |\mathbf{v}(\mathbf{q})|^2 \rangle$ in Fig. 4(c), all in the high chirality regime ($\Omega = 10$) and for noise strengths $D_r = 1, 10, 100$. We note that both the long-time $\langle \mathbf{r}^2 \rangle$ values and the $\langle |\mathbf{v}(\mathbf{q})|^2 \rangle$ curves exhibit non-monotonic behavior. However, the single particle $C_{\mathbf{vv}}$ result does not seem to capture this feature.

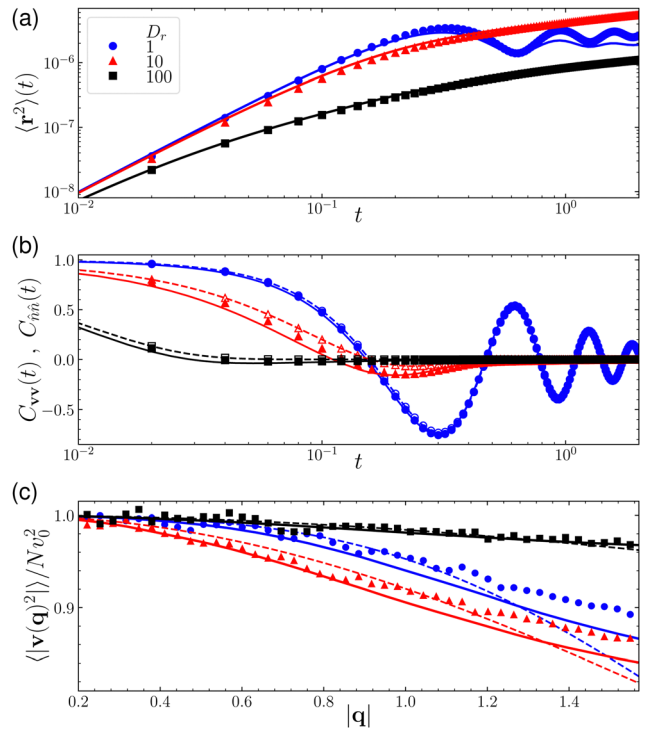

Fig. 4 Non-monotonic behavior (for high chirality and high noise) of chiral active solids as a function of noise D_r. (a) Mean-squared displacement $\langle \mathbf{r}^2 \rangle(t)$. The solid lines display analytical results recently obtained in ref. 89 for a single particle in a harmonic potential, given by eqn (28), as detailed in Appendix B. (b) Velocity and heading autocorrelation functions, $C_{\mathbf{vv}}(t) = \langle \mathbf{v}(t) \cdot \mathbf{v}(0) \rangle / \langle \mathbf{v}(0)^2 \rangle$ (filled symbols and solid lines) and $C_{\hat{n}\hat{n}}(t) = \langle \hat{n}(t) \cdot \hat{n}(0) \rangle$ (open symbols and dashed lines), as a function of time t. The solid lines result from the continuum elastic formulation in eqn (22) and the dashed lines correspond to plots of eqn (4). (c) Fourier space representation of $\langle |\mathbf{v}(\mathbf{q})^2| \rangle / N v_0^2$ as a function of $|\mathbf{q}|$. The solid lines result from the normal mode formulation in eqn (12) and the dashed lines are obtained from the continuum elastic formulation in eqn (18). In all panels, the symbols represent simulations and we fixed $v_0 = 0.01$ and $\Omega = 0.1$.

All these observations connect to the chiral glassy dynamics studied in ref. 89. In this work, the authors observe oscillatory temporal velocity autocorrelations and an emergent spatial correlation length in the limit of low D_r and low Ω, which we identify with the CMRO regime. They also find other states where the spatial correlations disappear but temporal correlations remain and a state without spatial or temporal correlations, corresponding to the CD and DD regimes, respectively. In the same study,[89] the authors discovered what they refer to as a 'hammering state', where particles oscillate in their potential cages, with a maximum in the mean-squared displacement (MSD) with respect to the diffusion constant. We can now identify this state with the maximum of the potential energy with respect to D_r, in the CD regime, as described analytically by our results.

6 Analysis of melting behavior at high activity

The solid to liquid transition in systems of active particles has been extensively studied, starting with the observation that, in the high density and low motility limit, active Brownian particles form crystals[99] if they are monodisperse and glasses otherwise.[100]

In a two-dimensional equilibrium crystal, the melting transition is a multifaceted process, characterized by the progressive disintegration of, both, positional and orientational coherence. In systems characterized by short-range interactions, melting manifests either as a first-order solid–liquid transition or *via* the sequential two-phase KTHNY mechanism involving solid–hexatic and hexatic–liquid transitions.[55,101–103] Unlike passive systems, active crystals can autonomously organize and transition into an active fluid state facilitated by self-propulsion and the interaction forces. In particular, however, the melting transition in active particle models of biological tissues occurs through a continuous solid–hexatic transition that is then followed by a continuous hexatic–liquid transition.[104,105]

The glass transition has been intensively studied in the context of active Brownian particles without chirality.[66,72,82,85,106] These efforts have shown that its differences with the usual thermal glass transition can be subtle, and that it is governed by an effective temperature $T_{eff} = v_0^2/2D_r$. This result only changes in the limit $D_r \to 0$,[107] where the coherent mesoscopic length scale becomes large[93,108] and starts influencing the transition properties.[86,106,109] On the other hand, glasses of chiral active particles have only been studied in detail up to now in ref. 89, and we discussed how this work connects to our results in the previous section.

We find in our simulation that, in the high activity limit, a solid triangular monocrystaline structure of chiral active

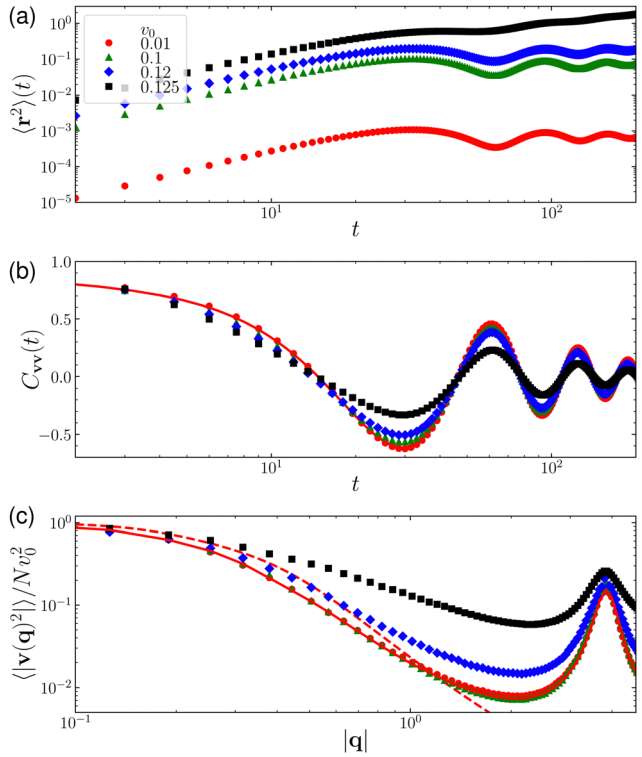

Fig. 5 Melting behavior of chiral active solids. The symbols result from simulations with different self-propulsion speed v_0 values, for $D_r = 0.01$ and $\Omega = 0.1$. (a) Mean-squared displacement $\langle \mathbf{r}^2 \rangle(t)$ as function of time t. (b) Velocity autocorrelation $C_{\mathbf{vv}}(t) = \langle \mathbf{v}(t) \cdot \mathbf{v}(0) \rangle / \langle \mathbf{v}(0)^2 \rangle$ as a function of time t. The solid line is obtained from the continuum elastic formulation in eqn (22). (c) Fourier space representation of $\langle |\mathbf{v}(\mathbf{q})^2| \rangle / N v_0^2$ as a function of $|\mathbf{q}|$. The solid line results from the normal mode formulation in eqn (12) and the dashed line, from the continuum elastic formulation in eqn (18).

particles will eventually melt. Since a detailed description of this transition would be beyond the scope of this work, we will focus instead on testing the tolerance of our analytic predictions to an increasing level of activity. Fig. 5 plots the numerical values of three different predicted quantities for increasing active speed v_0 levels. We consider fixed noise and chirality values that place the system in the CMRO regime, incrementally increasing v_0 to observe the melting behavior. The MSD exhibits trapped oscillatory behavior up to $v_0 = 0.12$, where melting begins, as shown in Fig. 5(a). The velocity autocorrelation functions in Fig. 5(b) and spatial velocity correlation functions in Fig. 5(c) also show that the deviation from the theory starts at $v_0 \gtrsim 0.1$. We include the corresponding dynamics of the velocity fields in the CMRO regime, with $D_r = 0.01$ and $\Omega = 0.1$, in the ESI,† (ref. 92) setting $v_0 = 0.1$ for Movie S6 and $v_0 = 0.12$ for Movie S7. These results clearly indicate that our analytic methods remain in excellent agreement with simulations until just below the melting transition, and that they start deviating at high activity. Nonetheless, we note that both the temporal oscillations and the mesoscale correlations persist, albeit with modified scaling. The latter is in agreement with what has been observed when fitting non-chiral models to cell sheet data[93] and in simulations of active Brownian particles (ABPs) at higher activity levels.[93,109] This also explains why our results can remain predictive for the active glassy dynamics investigated in ref. 89.

7 Extension to heterogeneous systems

We now extend our results to heterogeneous systems where the active particles can have different dynamical properties. We will first study binary mixtures of disks with different chirality and rotational diffusion coefficients in Section 7.1, and then cases where the disks have a distribution of chirality and diffusion values in Section 7.2.

7.1 Binary mixtures

We consider an active solid composed of two particle species, A and B, differentiated by their D_r and Ω values, and with corresponding packing fractions, ϕ_A and ϕ_B. Since the active driving produces time-correlated but spatially independent noise, as shown by eqn (7) and (16), the total driving noise from two species can be computed as a simple superposition, with no particle-particle cross-correlations. Then, quantities such as $\langle |\mathbf{v}(\mathbf{q})|^2 \rangle$ and $\langle \mathbf{v}(t) \cdot \mathbf{v}(0) \rangle$, which we analytically derived in Section 4, can be expressed as the mean of their A and B contributions, weighted by their respective fractions. In the linear response regime, the general expression for $f = |\mathbf{v}(\mathbf{q})|^2$ or for $f = \mathbf{v}(t) \cdot \mathbf{v}(0)$ is therefore given by

$$\langle f \rangle = \frac{\phi_A}{\phi} \langle f \rangle_A + \frac{(\phi - \phi_A)}{\phi} \langle f \rangle_B. \tag{23}$$

Here, $\langle \cdot \rangle_A$ and $\langle \cdot \rangle_B$ represent the mean over the A or B populations, respectively, and ϕ is the total packing fraction. We note that a mixture of positive and negative chiral active particles with the same absolute chirality but different signs behaves collectively just as a system with uniform chirality, due to the symmetry $\langle f \rangle_A(\Omega) = \langle f \rangle_B(-\Omega)$. Although spontaneous demixing can occur at low densities,[48] here the chiral active mixtures will remain fully mixed because of the high density and low active speed considered. However, the CMRO states will show the emergence of patches of uniform positive and negative chirality, in a proportion controlled by the ϕ_A/ϕ_B ratio (see Movie S8 in the ESI,† (ref. 92)). We also note that, for a random mixture of chiral active and passive particles with $v_0^A > 0$ and $v_0^B = 0$, the dynamics of the CMRO state is controlled by ϕ_A/ϕ.

To illustrate the effects of having binary mixtures of particles, we present simulations and analytical results for three different species combinations, all displaying chiral mesoscopic range order, in the CMRO regime. Fig. 6(a) and (b) respectively show the $C_{\mathbf{vv}}(t)$ and $\langle |\mathbf{v}(\mathbf{q})|^2 \rangle / N v_0^2$ curves obtained for three different binary mixtures with equal fractions ($\phi_A/\phi_B = 1$) and total packing fraction $\phi = 1$. First, the (i) curves show the single species case, as a reference. Second, the (ii) curves correspond to mixtures of achiral ($\Omega_A = 0$) and chiral ($\Omega_B = 0.1$) active particles with equal rotational diffusion coefficients $D_r^A = D_r^B = 0.01$. Third, the (iii) curves present mixtures of particles with two different chirality values, $\Omega_A = 0.1$ and $\Omega_B = 0.2$, and the same $D_r^A = D_r^B = 0.01$ (see also Movie S9 in the ESI,†

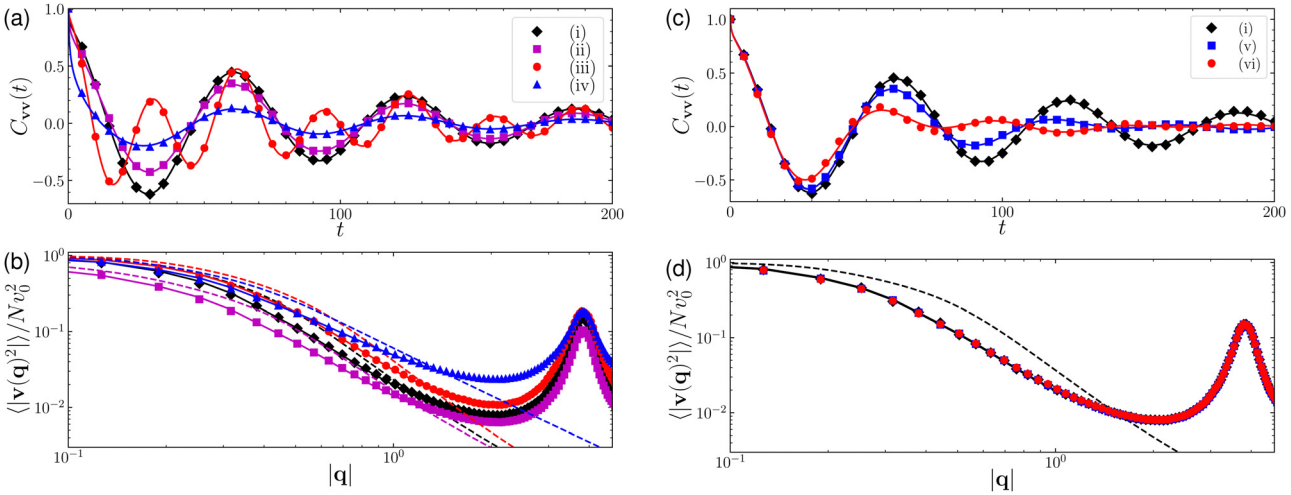

Fig. 6 Effects of heterogeneity in chiral active solids. (a) and (b) Binary mixtures of species A and B with packing fractions $\phi_A = \phi_B = 1/2$ for: (i) $D_r^A = D_r^B = 0.01$ and $\Omega_A = \Omega_B = 0.1$ (homogeneous case); (ii) $D_r^A = D_r^B = 0.01$, $\Omega_A = 0.0$, and $\Omega_B = 0.1$; (iii) $D_r^A = D_r^B = 0.01$, $\Omega_A = 0.1$, and $\Omega_B = 0.2$; and (iv) $D_r^A = 0.01$, $D_r^B = 0.1$, and $\Omega_A = \Omega_B = 0.1$. (c) and (d) Heterogeneous mixtures of particles with uniform distributions of (D_r,Ω) values spanning (v) ±20% and (vi) ±40% of their means, and homogeneous case (i) for comparison. In all panels, symbols represent numerical simulations. In panels (a) and (c), the solid lines plot the velocity autocorrelation $C_{\mathbf{vv}}(t)$ obtained from the continuum elastic formulation. In panels (b) and (d), the dashed and solid lines correspond to the mean-squared velocity $\langle|\mathbf{v}(\mathbf{q})|^2\rangle/Nv_0^2$ resulting respectively from the continuum elastic formulation and the normal mode formulation.

(ref. 92)). Finally, the (iv) curves display mixtures of particles with equal chirality values $\Omega_A = \Omega_B = 0.1$ and two different rotational diffusion coefficients, $D_r^A = 0.01$ and $D_r^B = 0.1$.

In Fig. 6(a) we can see that the clear oscillations in the velocity autocorrelation are suppressed when we consider achiral–chiral mixtures (ii), compared to the single species case (i). We can also see that, in systems with two different chirality values (iii), the velocity autocorrelation function displays oscillations with the two corresponding periods, $2\pi/\Omega_A$ and $2\pi/\Omega_B$. Finally, the figure shows that mixtures of chiral active particles with two different rotational diffusion coefficients (iv) suppress this oscillatory behavior and follow the lower persistence length of the population with the highest D_r. In Fig. 6(b) we can see that binary mixtures of achiral and chiral active particles (ii) enhance the ordering in the CMRO state when compared to the homogeneous case (i), decaying at lower $|\mathbf{q}|$ values. On the other hand, we see that chiral active binary mixtures with, both, different chirality values (iii) and different rotational diffusion coefficients (iv) suppress the ordering in the CMRO state when compared to the homogeneous case (i), decaying at larger $|\mathbf{q}|$ values. In addition, we note that the analytic superposition results (solid and dashed lines) show an excellent agreement with the simulation results (symbols) for all curves in Fig. 6(a) and (b), thus validating eqn (23).

Finally, Fig. S4 in the ESI,† (ref. 92) further illustrates how oscillations appear, disappear, and interfere by presenting the velocity time correlations obtained from eqn (23) for a range of binary mixtures.

7.2 Heterogeneous particles

We now further extend our analyses to investigate active solids composed of heterogeneous particles with a distribution of dynamical properties. To do this, we consider a complex random mixture of n different types of active particles, each with corresponding packing fraction $\phi_1,\phi_2,\ldots,\phi_n$, adding up to a total packing fraction $\phi = \sum_{i=1}^{n} \phi_i$. We can then obtain a general expression for the combined values of $f = |\mathbf{v}(\mathbf{q})|^2$ or $f = \mathbf{v}(t)\cdot\mathbf{v}(0)$ in terms of the individual components as

$$\langle f \rangle = \sum_{i=1}^{n} \phi_i \langle f \rangle_i / \phi, \tag{24}$$

where $\langle\cdot\rangle_i$ represents the mean over population type i. With this general superposition expression, we can analytically predict the dynamics of an active solid composed of any combination of active particles, in the linear response regime.

Fig. 6(c) and (d) present the analytical and simulated spatiotemporal correlation functions of the active solid dynamics of a set of particles with a uniformly distributed range of D_r and Ω values, spanning: (i) ±0%, (v) ±20%, and (vi) ±40% with respect to their mean $\langle(D_r,\Omega)\rangle = (0.01,0.1)$. We can see in Fig. 6(c) a clear deviation of the velocity–velocity correlations $C_{\mathbf{vv}}$ in the heterogeneous cases, (v) and (vi), with respect to the homogeneous case (i). We note that the analytical superposition of eqn (22) using eqn (24), displayed as solid lines, perfectly captures the simulation results, represented by symbols. In Fig. 6(d), we see that $\langle|\mathbf{v}(\mathbf{q})|^2\rangle/Nv_0^2$ is practically invariant under changes in the D_r and Ω parameters. We also note that the analytical superposition of eqn (12) and (18), represented respectively by a solid and a dashed line, can properly capture our simulation results. The figure shows that the spatial velocity correlations are insensitive to the heterogeneity of the system, but that the temporal velocity autocorrelation is affected by it. Indeed, increased heterogeneity in particle chirality leads to a desynchronization of the oscillations, while increased heterogeneity in D_r does not (as shown in

Fig. S5a and c in the ESI,† (ref. 92)). The spatial correlations are not affected in either case (see Fig. S5b and d in the ESI,† (ref. 92)). We can thus predict that the oscillatory dynamics will only be apparent in systems of active particles with relatively homogeneous levels of chirality.

8 Conclusions

In this work, we formulated the analytic linear response theory for an active solid composed of self-propelled particles with noisy chiral dynamics. We considered a minimal model with the potential for describing a broad range of systems, ranging from artificial active solids made of chiral self-propelled robots to biological tissues with emergent macroscopic chiral order. We developed an analytic formulation that allowed us to fully describe all the observed dynamics in the linear regime, perfectly matching our numerical results.

We described the emergence of four different types of dynamics in the phase space described by the chirality Ω and the rotational diffusion coefficient D_r. For small enough D_r and Ω, we observe chiral (CMRO) and achiral (MRO) self-organized states displaying mesoscopic range order. For larger D_r and Ω, we only find chiral (CD) and achiral (DD) disordered states. In all cases, the chiral sates appear for $D_r < \Omega$ and the achiral states, for $D_r > \Omega$. We then explored the dynamics of the melting regime by increasing the activity v_0, showing that our analytic results for the spatial velocity correlations and the temporal velocity autocorrelations agree with simulations up to an active speed $v_0 \approx 0.1$, just below $v_0 = 0.12$, the melting point obtained using our active solid theory. Finally, we showed that our analytic approaches can be extended to consider particles with heterogeneous dynamical features, including different chirality and rotational diffusion levels. We derived analytic superposition expressions for binary and more complex mixtures of heterogeneous active particles, demonstrating their excellent agreement with simulations.

Our work is consistent with the (relatively sparse) literature on chiral ABP solids. Notably we recover the oscillatory correlations and 'hammering' resonance observed by Debets *et al.*[89] in the glassy state. In addition, our work also seems to be consistent with recent results obtained by Caprini *et al.*[90] while exploring the emergence of self-reverting vortices in the absence of alignment forces, as a result of the interplay between attractive interactions and chirality. They found two kinds of vortices, with either persistent or oscillatory behavior, which could correspond to our observation that the correlated velocity fields in the mesoscopic range can either be persistent (MRO) or oscillatory (CMRO). However, due to subtle differences in the equations (that include inertia and spatial noise in their case), we cannot currently compare our results quantitatively.

There are various possible extensions to our framework. We could, for example, introduce hydrodynamic interactions, which would modify our findings. It is indeed relatively straightforward to add a mobility matrix to the spatial equation, *e.g.* through a pair dissipation term $\lambda(\mathbf{v}_i - \mathbf{v}_j)$, where λ is the ratio of pair to single particle friction. This leads to yet another modified mesoscopic length scale that is basically the hydrodynamic length scale $l_H = \sqrt{\lambda l_0^2}$. However, wet hydrodynamic interactions also introduce torque couplings between particles, which invalidates our linear response approach, as the angular equation cannot be solved independently anymore. Although this will likely lead to very interesting collective phenomenology, similar to that in ref. 50 and 51, such analysis is still beyond our reach.

We hope that the general analytical description of dense, solid chiral dry active systems in this paper can help establish the foundations for a systematic understanding of the emergent dynamics in this type of systems. Future research could explore the scalability of our theory, its practical applications in synthetic biology, and its potential impact on the design and control of rotating correlated velocity fields in natural or artificial active solids.

Author contributions

Conceptualization: Amir Shee, Silke Henkes, and Cristián Huepe; analytic calculations and numerical simulations: Amir Shee; writing – original draft preparation: Amir Shee; writing – review and editing: Amir Shee, Silke Henkes, and Cristián Huepe; supervision: Silke Henkes and Cristián Huepe.

Data availability

The data supporting this article have been included as part of the ESI.† All relevant datasets have been archived and can be provided for replication and further research purposes.

Conflicts of interest

There are no conflicts to declare.

Appendices

A. Orientation autocorrelation

We adopt the method for the exact moments calculation of stiff chains described in Hermans *et al.*[110] to determine the moments for the active dynamics case. This approach, previously applied in,[111–113] is used to obtain the exact dynamics for a chiral active Brownian particle in a harmonic trap, as detailed in Debets *et al.*[89] Utilizing the Laplace transform $\tilde{P}(\hat{n}, s) = \int_0^\infty \mathrm{d}t e^{-st} P(\hat{n}, t)$ in eqn (3) while defining the mean of an observable as $\langle\psi\rangle_s = \int \mathrm{d}\hat{n}\psi(\hat{n})\tilde{P}(\hat{n}, s)$, multiplying by $\psi(\hat{n})$, and integrating over all possible $\hat{n}$, we find

$$-\langle\psi\rangle_0 + s\langle\psi\rangle_s = D_r\langle\nabla_{\hat{n}}{}^2\psi\rangle_s + \Omega\langle\hat{n}^\perp\cdot\nabla_{\hat{n}}\psi\rangle_s. \qquad (25)$$

Here, the initial condition sets $\langle\psi\rangle_0 = \int \mathrm{d}\hat{n}\psi(\hat{n})P(\hat{n}, 0)$. Without loss of generality, we can define the initial condition as following $P(\hat{n},0) = \delta(\hat{n} - \hat{n}_0)$, where $\hat{n}_0$ is the initial orientation of the particle.

Using eqn (25), we compute the orientational correlation as a function of time. We set the initial particle headings as satisfying $\langle \hat{n} \rangle = \hat{n}_0$. To compute $\langle \hat{n} \rangle$, we then use $\psi = \hat{n}$ in eqn (25) to obtain

$$\langle \hat{n} \rangle_s = \frac{\hat{n}_0 + \Omega \langle \hat{n}^\perp \rangle_s}{s + D_r}. \tag{26}$$

Here, we can find $\langle \hat{n}^\perp \rangle_s$, starting from an initial perpendicular orientation $\langle \hat{n}^\perp \rangle = \hat{n}_0^\perp$, by using $\psi = \hat{n}^\perp$ in eqn (25), which gives $\langle \hat{n}^\perp \rangle_s = (\hat{n}_0^\perp - \Omega \langle \hat{n} \rangle_s)/(s + D_r)$. Substituting back into eqn (26) produces

$$\langle \hat{n} \rangle_s = \frac{\hat{n}_0 (s + D_r) + \Omega \hat{n}_0^\perp}{(s + D_r)^2 + \Omega^2}. \tag{27}$$

An inverse Laplace transform then leads to $\langle \hat{n}(t) \rangle = e^{-D_r t}[\hat{n}_0 \cos(\Omega t) + \hat{n}_0^\perp \sin(\Omega t)]$. Finally, by computing the dot product with the initial heading, we find the orientation autocorrelation expression in eqn (4).

B. Single chiral active Brownian particle in a harmonic trap

Following procedure similar to that used in the orientation autocorrelation calculation, we can compute the MSD of a single chiral active Brownian particle in a harmonic trap, as previously done in ref. 89, finding

$$\begin{aligned} &\langle \mathbf{r}^2 \rangle(t) \\ &= \frac{v_0^2 (D_r + \mu k)}{\mu k \left[(D_r + \mu k)^2 + \Omega^2 \right]} - \frac{v_0^2 (D_r - \mu k) e^{-2\mu k t}}{\mu k \left[(D_r - \mu k)^2 + \Omega^2 \right]} \\ &\quad + \frac{2 v_0^2 e^{-(D_r + \mu k)t} \left[\left(D_r^2 - \mu^2 k^2 - \Omega^2 \right) \cos(\Omega t) - 2 D_r \Omega \sin(\Omega t) \right]}{\left[(D_r - \mu k)^2 + \Omega^2 \right] \left[(D_r + \mu k)^2 + \Omega^2 \right]}. \end{aligned} \tag{28}$$

We plot this expression in Fig. 4(a) to compare it to the MSD of dense chiral active systems in the high D_r, high Ω regime, showing that it follows a similar behavior. Simplifying eqn (28) in the $D_r t \ll 1$, $\Omega t \ll 1$ limit yields

$$\begin{aligned} \langle \mathbf{r}^2 \rangle(t) &= v_0^2 t^2 - \frac{v_0^2}{3} (D_r + 3\mu k) t^3 \\ &\quad + \frac{v_0^2}{12} \left(D_r^2 + 4 D_r \mu k + 7 \mu^2 k^2 - \Omega^2 \right) t^4 + \mathcal{O}\left(t^5 \right). \end{aligned} \tag{29}$$

We can then compute the steady-state MSD as $\langle \mathbf{r}^2 \rangle_{st} = \langle \mathbf{r}^2 \rangle(t)|_{t \to \infty}$, to obtain

$$\langle \mathbf{r}^2 \rangle_{st} = \frac{v_0^2 (D_r + \mu k)}{\mu k \left[(D_r + \mu k)^2 + \Omega^2 \right]}. \tag{30}$$

The $\langle \mathbf{r}^2 \rangle_{st}$ value will thus have a maximum (for constant Ω) along the $D_r^* = \Omega - \mu k$ line, shown as the black dotted line on the $D_r - \Omega$ plane in Fig. 1(a), for $\mu = 1$ and $k = 1$. This suggests that the reentrant transition with increasing D_r (from low $\langle \mathbf{r}^2 \rangle_{st}$ to high $\langle \mathbf{r}^2 \rangle_{st}$, with maximum at D_r^*, and then back to low $\langle \mathbf{r}^2 \rangle_{st}$) occurs only when chirality is high, that is, for $\Omega > \mu k$.

C. Determining the elastic moduli and continuum theory to compare with simulations

To determine the elastic moduli, we first equilibrate the steady state configurations by letting $v_0 = 0$ in eqn (1). The disks reach their equilibrium positions after a long integration time. Using these positions, we then construct a dynamical Hessian matrix. We transform this matrix to Fourier space with appropriate grid space $\mathbf{q}$. The resulting longitudinal and transverse eigenvalues thus correspond to $(B + G)q^2$ and Gq^2, respectively. We then determine the bulk modulus B and shear modulus G by performing a linear fit of the radially averaged longitudinal and transverse eigenvalues against q^2, focusing on the limit with $q^2 \leq 1$. Our calculations for soft disks thus yield the following values for the moduli: : $G = 0.61$, $B = 2.03$, and $(B + G)/G = 4.33$, with relative error lower than 1% (averaging over 10 independent estimations).

When comparing our numerical results to the continuum theory, simulations are carried out for relatively large but finite systems of size L, with minimum length scale given by the particle size $a = 2r_0$, where r_0 is the particle radius. Our numerical analysis is therefore performed using discrete Fourier transforms, in a finite grid, whereas our analytical calculations are carried out in the continuum limit, by setting $L \to \infty$ and $a \to 0$.

Finally, to achieve consistency between the discrete and continuum approaches, we use the following continuous Fourier transform

$$\mathbf{u}(\mathbf{r}, t) = \frac{1}{(2\pi)^2} \int \mathrm{d}^2 \mathbf{q} \tilde{\mathbf{u}}(\mathbf{q}, t) e^{-i \mathbf{q} \cdot \mathbf{r}}. \tag{31}$$

Then, by considering the finite system and particle sizes, we discretize the integral into

$$\frac{1}{(2\pi)^2} \int \mathrm{d}^2 \mathbf{q} \to \frac{1}{N a^2} \sum_{\mathbf{q}} \text{ and } \int \mathrm{d}^2 \mathbf{r} \to a^2 \sum_r,$$

where $N = 4\phi L^2/\pi a^2$ and ϕ is the packing fraction of the system (close to 1 for dense systems). In the sum, $\mathbf{q}$ takes discrete values defined by the geometry of the system. For instance, for a square lattice of linear size L, $\mathbf{q} \equiv (q_x, q_y) = 2\pi/L(m,n)$, with integers m, n satisfying $0 \leq m,n \leq L/a - 1$. Thus, the discrete space Fourier transform $\mathbf{u}(\mathbf{q},t)$ is related to the continuous Fourier transform $\tilde{\mathbf{u}}(\mathbf{q},t)$ *via* $\tilde{\mathbf{u}}(\mathbf{q},t) = a^2 \mathbf{u}(\mathbf{q},t)$.

Acknowledgements

This project was made possible through the support of Grant 62213 from the John Templeton Foundation. SH would like to acknowledge support of the NWO through her Leiden University startup package within the sector plan.

Notes and references

1 F. Kümmel, B. ten Hagen, R. Wittkowski, I. Buttinoni, R. Eichhorn, G. Volpe, H. Löwen and C. Bechinger, *Phys. Rev. Lett.*, 2013, **110**, 198302.

2 C. Bechinger, R. Di Leonardo, H. Löwen, C. Reichhardt, G. Volpe and G. Volpe, *Rev. Mod. Phys.*, 2016, **88**, 45006.
3 T. Mano, J. B. Delfau, J. Iwasawa and M. Sano, *Proc. Natl. Acad. Sci. U. S. A.*, 2017, **114**, E2580–E2589.
4 B. Zhang and A. Snezhko, *Phys. Rev. Lett.*, 2022, **128**, 218002.
5 B. A. Grzybowski, H. A. Stone and G. M. Whitesides, *Nature*, 2000, **405**(6790), 1033–1036.
6 J.-M. Cruz, O. Díaz-Hernández, A. Castañeda-Jonapá, G. Morales-Padrón, A. Estudillo and R. Salgado-García, *Soft Matter*, 2024, **20**, 1199–1209.
7 H. S. Jennings, *Am. Nat.*, 1901, **35**, 369–378.
8 M. Loose and T. J. Mitchison, *Nat. Cell Biol.*, 2014, **16**, 38–46.
9 Y. Sumino, K. H. Nagai, Y. Shitaka, D. Tanaka, K. Yoshikawa, H. Chaté and K. Oiwa, *Nature*, 2012, **483**, 448–452.
10 C. J. Brokaw, D. J. Luck and B. Huang, *J. Cell Biol.*, 1982, **92**, 722–732.
11 W. R. DiLuzio, L. Turner, M. Mayer, P. Garstecki, D. B. Weibel, H. C. Berg and G. M. Whitesides, *Nature*, 2005, **435**, 1271–1274.
12 E. Lauga, W. R. DiLuzio, G. M. Whitesides and H. A. Stone, *Biophys. J.*, 2006, **90**, 400–412.
13 I. H. Riedel, K. Kruse and J. Howard, *Science*, 2005, **309**, 300–303.
14 R. Nosrati, A. Driouchi, C. M. Yip and D. Sinton, *Nat. Commun.*, 2015, **6**, 8703.
15 S. van Teeffelen and H. Löwen, *Phys. Rev. E: Stat., Nonlinear, Soft Matter Phys.*, 2008, **78**, 020101.
16 S. Van Teeffelen, U. Zimmermann and H. Löwen, *Soft Matter*, 2009, **5**, 4510–4519.
17 M. Mijalkov and G. Volpe, *Soft Matter*, 2013, **9**, 6376–6381.
18 G. Volpe, S. Gigan and G. Volpe, *Am. J. Phys.*, 2014, **82**, 659–664.
19 H. Löwen, *Eur. Phys. J.: Spec. Top.*, 2016, **225**, 2319–2331.
20 F. J. Sevilla, *Phys. Rev. E*, 2016, **94**, 062120.
21 T. Markovich, E. Tjhung and M. E. Cates, *New J. Phys.*, 2019, **21**, 112001.
22 O. Chepizhko and T. Franosch, *New J. Phys.*, 2020, **22**, 073022.
23 L. Caprini, H. Löwen and U. Marini Bettolo Marconi, *Soft Matter*, 2023, **19**, 6234–6246.
24 R. Di Leonardo, D. Dell'Arciprete, L. Angelani and V. Iebba, *Phys. Rev. Lett.*, 2011, **106**, 038101.
25 G. Araujo, W. Chen, S. Mani and J. X. Tang, *Biophys. J.*, 2019, **117**, 346–354.
26 M. Böhmer, Q. Van, I. Weyand, V. Hagen, M. Beyermann, M. Matsumoto, M. Hoshi, E. Hildebrand and U. B. Kaupp, *EMBO J.*, 2005, **24**, 2741–2752.
27 J. Taktikos, V. Zaburdaev and H. Stark, *Phys. Rev. E: Stat., Nonlinear, Soft Matter Phys.*, 2011, **84**, 41924.
28 J. G. Gibbs and Y. Zhao, *Small*, 2009, **5**, 2304–2308.
29 J. G. Gibbs, S. Kothari, D. Saintillan and Y.-P. Zhao, *Nano Lett.*, 2011, **11**, 2543–2550.
30 J. Denk, L. Huber, E. Reithmann and E. Frey, *Phys. Rev. Lett.*, 2016, **116**, 178301.
31 M. Bär, R. Großmann, S. Heidenreich and F. Peruani, *Annu. Rev. Condens. Matter Phys.*, 2020, **11**, 441–466.
32 B. Zhang, A. Sokolov and A. Snezhko, *Nat. Commun.*, 2020, **11**, 4401.
33 A. I. Campbell, R. Wittkowski, B. Ten Hagen, H. Löwen and S. J. Ebbens, *J. Chem. Phys.*, 2017, **147**, 84905.
34 R. J. Archer, A. I. Campbell and S. J. Ebbens, *Soft Matter*, 2015, **11**, 6872–6880.
35 T. Lei, C. Zhao, R. Yan and N. Zhao, *Soft Matter*, 2023, **19**, 1312–1329.
36 B. Liebchen and D. Levis, *Phys. Rev. Lett.*, 2017, **119**, 058002.
37 D. Levis and B. Liebchen, *J. Phys.: Condens. Matter*, 2018, **30**, 084001.
38 G. J. Liao and S. H. Klapp, *Soft Matter*, 2018, **14**, 7873–7882.
39 A. Kaiser and H. Löwen, *Phys. Rev. E: Stat., Nonlinear, Soft Matter Phys.*, 2013, **87**, 032712.
40 Y. Liu, Y. Yang, B. Li and X.-Q. Feng, *Soft Matter*, 2019, **15**, 2999–3007.
41 Z. Ma and R. Ni, *J. Chem. Phys.*, 2022, **156**, 21102.
42 V. Semwal, J. Joshi and S. Mishra, *Phys. A*, 2024, **634**, 129435.
43 J. Bickmann, S. Bröker, J. Jeggle and R. Wittkowski, *J. Chem. Phys.*, 2022, **156**, 194904.
44 Q.-L. Lei and R. Ni, *Proc. Natl. Acad. Sci. U. S. A.*, 2019, **116**, 22983–22989.
45 Q.-L. Lei, M. P. Ciamarra and R. Ni, *Sci. Adv.*, 2019, **5**, eaau7423.
46 B. Hrishikesh and E. Mani, *Soft Matter*, 2023, **19**, 225–232.
47 D. Levis and B. Liebchen, *Phys. Rev. E*, 2019, **100**, 012406.
48 B.-Q. Ai, S. Quan and F. G. Li, *New J. Phys.*, 2023, **25**, 063025.
49 S. Ceron, K. O'Keeffe and K. Petersen, *Nat. Commun.*, 2023, **14**, 940.
50 E. S. Bililign, F. Balboa Usabiaga, Y. A. Ganan, A. Poncet, V. Soni, S. Magkiriadou, M. J. Shelley, D. Bartolo and W. T. Irvine, *Nat. Phys.*, 2022, **18**, 212–218.
51 T. H. Tan, A. Mietke, J. Li, Y. Chen, H. Higinbotham, P. J. Foster, S. Gokhale, J. Dunkel and N. Fakhri, *Nature*, 2022, **607**, 287–293.
52 K. Drescher, K. C. Leptos, I. Tuval, T. Ishikawa, T. J. Pedley and R. E. Goldstein, *Phys. Rev. Lett.*, 2009, **102**, 168101.
53 A. P. Petroff, X.-L. Wu and A. Libchaber, *Phys. Rev. Lett.*, 2015, **114**, 158102.
54 J. Yan, S. C. Bae and S. Granick, *Soft Matter*, 2015, **11**, 147–153.
55 Z.-F. Huang, A. M. Menzel and H. Löwen, *Phys. Rev. Lett.*, 2020, **125**, 218002.
56 T. Ishikawa, T. J. Pedley, K. Drescher and R. E. Goldstein, *J. Fluid Mech.*, 2020, **903**, A11.
57 A. P. Petroff, C. Whittington and A. Kudrolli, *Phys. Rev. E*, 2023, **108**, 014609.
58 M. Fruchart, C. Scheibner and V. Vitelli, *Annu. Rev. Condens. Matter Phys.*, 2023, **14**, 471–510.
59 S. Henkes, Y. Fily and M. C. Marchetti, *Phys. Rev. E: Stat., Nonlinear, Soft Matter Phys.*, 2011, **84**, 040301.

60 G. Lin, Z. Han and C. Huepe, *New J. Phys.*, 2021, **23**, 023019.
61 P. Baconnier, D. Shohat, C. H. López, C. Coulais, V. Démery, G. Düring and O. Dauchot, *Nat. Phys.*, 2022, **18**, 1234–1239.
62 G. Lin, Z. Han, A. Shee and C. Huepe, *Phys. Rev. Lett.*, 2023, **131**, 168301.
63 P. Baconnier, D. Shohat and O. Dauchot, *Phys. Rev. Lett.*, 2023, **130**, 028201.
64 H. Xu, Y. Huang, R. Zhang and Y. Wu, *Nat. Phys.*, 2023, **19**, 46–51.
65 L. Berthier and J. Kurchan, *Nat. Phys.*, 2013, **9**, 310–314.
66 L. Berthier, *Phys. Rev. Lett.*, 2014, **112**, 220602.
67 G. Szamel, E. Flenner and L. Berthier, *Phys. Rev. E: Stat., Nonlinear, Soft Matter Phys.*, 2015, **91**, 062304.
68 V. E. Debets and L. M. C. Janssen, *J. Chem. Phys.*, 2023, **159**, 14502.
69 R. Ni, M. A. C. Stuart and M. Dijkstra, *Nat. Commun.*, 2013, **4**, 2704.
70 D. Bi, X. Yang, M. C. Marchetti and M. L. Manning, *Phys. Rev. X*, 2016, **6**, 021011.
71 A. Liluashvili, J. Ónody and T. Voigtmann, *Phys. Rev. E*, 2017, **96**, 062608.
72 S. K. Nandi, R. Mandal, P. J. Bhuyan, C. Dasgupta, M. Rao and N. S. Gov, *Proc. Natl. Acad. Sci. U. S. A.*, 2018, **115**, 7688–7693.
73 G. Szamel, *J. Chem. Phys.*, 2019, **150**, 124901.
74 R. Mandal and P. Sollich, *Phys. Rev. Lett.*, 2020, **125**, 218001.
75 J. Reichert, S. Mandal and T. Voigtmann, *Phys. Rev. E*, 2021, **104**, 044608.
76 J. Reichert and T. Voigtmann, *Soft Matter*, 2021, **17**, 10492–10504.
77 J. Reichert, L. F. Granz and T. Voigtmann, *Eur. Phys. J. E: Soft Matter Biol. Phys.*, 2021, **44**, 27.
78 V. E. Debets, X. M. de Wit and L. M. Janssen, *Phys. Rev. Lett.*, 2021, **127**, 278002.
79 V. E. Debets and L. M. C. Janssen, *Phys. Rev. Res.*, 2022, **4**, L042033.
80 G. Janzen and L. M. C. Janssen, *Phys. Rev. Res.*, 2022, **4**, L012038.
81 M. Paoluzzi, D. Levis and I. Pagonabarraga, *Commun. Phys.*, 2022, **5**, 111.
82 E. Flenner, G. Szamel and L. Berthier, *Soft Matter*, 2016, **12**, 7136–7149.
83 G. Szamel, *Phys. Rev. E*, 2016, **93**, 012603.
84 M. Feng and Z. Hou, *Soft Matter*, 2017, **13**, 4464–4481.
85 L. Berthier, E. Flenner and G. Szamel, *New J. Phys.*, 2017, **19**, 125006.
86 E. Flenner and G. Szamel, *Phys. Rev. E*, 2020, **102**, 022607.
87 L. Caprini and U. Marini Bettolo Marconi, *Soft Matter*, 2021, **17**, 4109–4121.
88 G. Szamel and E. Flenner, *Europhys. Lett.*, 2021, **133**, 60002.
89 V. E. Debets, H. Löwen and L. M. Janssen, *Phys. Rev. Lett.*, 2023, **130**, 058201.
90 L. Caprini, B. Liebchen and H. Löwen, *Commun. Phys.*, 2024, **7**, 153.
91 Y. Kuroda, T. Kawasaki and K. Miyazaki, *arXiv*, 2024, preprint, arXiv:2402.19192, DOI: **10.48550/arXiv.2402.19192**.
92 See ESI† at **https://doi.org/10.1039/D4SM00958D** for description of simulation movies, analytic calculations, which include ref. 93 and 114.
93 S. Henkes, K. Kostanjevec, J. M. Collinson, R. Sknepnek and E. Bertin, *Nat. Commun.*, 2020, **11**, 1405.
94 L. Caprini and U. Marini Bettolo Marconi, *Soft Matter*, 2019, **15**, 2627–2637.
95 K. Chen, W. G. Ellenbroek, Z. Zhang, D. T. Chen, P. J. Yunker, S. Henkes, C. Brito, O. Dauchot, W. Van Saarloos, A. J. Liu and A. G. Yodh, *Phys. Rev. Lett.*, 2010, **105**, 025501.
96 S. Henkes, C. Brito and O. Dauchot, *Soft Matter*, 2012, **8**, 6092.
97 J. Melio, S. E. Henkes and D. J. Kraft, *Phys. Rev. Lett.*, 2024, **132**, 078202.
98 S. Garcia, E. Hannezo, J. Elgeti, J.-F. Joanny, P. Silberzan and N. S. Gov, *Proc. Natl. Acad. Sci. U. S. A.*, 2015, **112**, 15314–15319.
99 J. Bialké, T. Speck and H. Löwen, *Phys. Rev. Lett.*, 2012, **108**, 168301.
100 Y. Fily, S. Henkes and M. C. Marchetti, *Soft Matter*, 2014, **10**, 2132–2140.
101 J. G. Dash, *Rev. Mod. Phys.*, 1999, **71**, 1737–1743.
102 U. Gasser, *J. Phys.: Condens. Matter*, 2009, **21**, 203101.
103 Y.-W. Li and M. P. Ciamarra, *Phys. Rev. Lett.*, 2020, **124**, 218002.
104 P. Digregorio, D. Levis, A. Suma, L. F. Cugliandolo, G. Gonnella and I. Pagonabarraga, *Phys. Rev. Lett.*, 2018, **121**, 098003.
105 A. Pasupalak, L. Yan-Wei, R. Ni and M. Pica Ciamarra, *Soft Matter*, 2020, **16**, 3914–3920.
106 L. Berthier, E. Flenner and G. Szamel, *J. Chem. Phys.*, 2019, **150**, 200901.
107 R. Mandal, P. J. Bhuyan, P. Chaudhuri, C. Dasgupta and M. Rao, *Nat. Commun.*, 2020, **11**, 2581.
108 L. Caprini, U. M. B. Marconi, C. Maggi, M. Paoluzzi and A. Puglisi, *Phys. Rev. Res.*, 2020, **2**, 023321.
109 Y.-E. Keta, J. U. Klamser, R. L. Jack and L. Berthier, *Phys. Rev. Lett.*, 2024, **132**, 218301.
110 J. Hermans and R. Ullman, *Physica*, 1952, **18**, 951–971.
111 A. Shee, A. Dhar and D. Chaudhuri, *Soft Matter*, 2020, **16**, 4776–4787.
112 D. Chaudhuri and A. Dhar, *J. Stat. Mech.: Theory Exp.*, 2021, **2021**, 013207.
113 A. Shee and D. Chaudhuri, *J. Stat. Mech.: Theory Exp.*, 2022, **2022**, 013201.
114 P. M. Chaikin and T. C. Lubensky, *Principles of Condensed Matter Physics*, Cambridge University Press, Cambridge, 1995.